Article

Hydrothermal Mineralization and Mineral Chemistry of Arsenides and Sulfarsenides in the Fe-Co-Ni-As-S System and Introduction of Three Unique Minerals, Port Radium Deposit, Canada

Alireza K. Somarin [1,*], **Li Zhou** [2,3], **Guodong Zheng** [4,5] and **Xiangxian Ma** [4,5]

1   Department of Geology, Brandon University, Brandon, MB R7A 6A9, Canada
2   School of Geography and Environmental Science, Guizhou Normal University, Guiyang 550025, China; zhouli@gznu.edu.cn
3   Key Laboratory of High-Temperature and High-Pressure Study of the Earth's Interior, Institute of Geochemistry, Chinese Academy of Sciences, Guiyang 550081, China
4   Northwest Institute of Eco-Environment and Resources, Chinese Academy of Sciences, Lanzhou 730000, China; gdzhbj@mail.iggcas.ac.cn (G.Z.); maxxan04@163.com (X.M.)
5   Key Laboratory of Petroleum Resources, Lanzhou 730000, China
*   Correspondence: somarina@brandonu.ca; Tel.: +1-204-727-9686

Abstract: The Port Radium U-Cu-Ni-Co-Ag deposit in northwestern Canada is hosted within a mineral system that has generated a variety of mineralization styles from iron oxide-copper-gold to iron oxide-apatite, porphyry, skarn, and epithermal. Their genesis is linked to an extensive subduction-related magmatism that formed widespread dacite-rhyodacite-andesite volcanic and volcanoclastic sequences (~1.87 Ga), which have been intruded by their equivalent intrusive plutons. Pervasive and intensive hydrothermal alterations, including albitic, magnetite-actinolite-apatite, potassic $\pm$ albitic, phyllic, and propylitic occurred before the main sulfide, sulfarsenide, and uraninite vein-type mineralization. Although scarce sulfide minerals formed at the beginning of the hydrothermal activity, the main polymetallic arsenide-sulfarsenide-sulfide $\pm$ uraninite vein-type mineralization occurred during the epithermal stage. In addition to the common arsenides and sulfarsenides including nickeline, cobaltite, rammelsbergite, safflorite, skutterudite, gersdorffite, and arsenopyrite, three unique sulfarsenides were also found: $Co_{0.67}Ni_{0.32}Fe_{0.02}S_{0.19}As_{2.80}$, which could be a sulfur-rich skutterudite, $Ni_{0.85}Co_{0.15}S_{0.39}As_{1.60}$, and $Ni_{0.69}Co_{0.31}S_{0.47}As_{1.52}$, which are chemically comparable to the Port Radium rammelsbergite with substantial addition of S and Co; they could be the solid solution product of gersdorffite-cobaltite or safflorite-rammelsbergite.

Keywords: Great Bear magmatic zone; Port Radium; Mag Hill; Fe-Co-Ni-As-S system; sulfarsenides; mineral chemistry

1. Introduction

Arsenides and sulfarsenides of the Fe-Co-Ni-As-S system form a diverse group of ore minerals that are commonly found in magmatic sulfide (i.e., genetically directly related to igneous processes) and hydrothermal vein deposits (i.e., genetically may or may not be related to igneous processes) worldwide, e.g., [1–7]. Minerals of this system have been studied in synthetic samples to natural occurrences for several decades, e.g., [5,8–13]. Each work has elucidated only part of this complicated system because there is no single ore deposit that has all possible mineral variations in this system. Polymorphism and extensive substitution of Fe-Co-Ni in the cation site and As-S in the anion site add to the complexity of minerals in this system.

The Port Radium deposit is located in the Great Bear magmatic zone (GBMZ) in northwestern Canada. This continental magmatic arc is part of the Wopmay orogen, which

outcrops 450 km from Great Bear Lake to Great Slave Lake in the Northwest Territories, Canada [14]. The zone consists mainly of felsic-intermediate volcanic rocks intruded by various granitic plutons during the 1.87 to 1.85 Ga magmatic arc activity [15–19]. As a result, a wide range of mineralization styles formed, notably iron oxide-copper-gold (IOCG), iron oxide-apatite (IOA), skarn, porphyry, metasomatic iron-cobalt, albitite-hosted uranium, and five-element epithermal veins [20–23]. Several papers have been published on the regional geology, alteration facies, and deposit types of the area, e.g., [14,15,20,22,24–26]. However, detailed mineralogical studies of the Port Radium deposit and field relationship between various alteration zones are rare, e.g., [27] even though the vein-style mineralization was studied in detail in the adjacent Camsell River district [28]. Field mapping and core logging of tens of drill holes (with several km of cores in total length) from Port Radium and surrounding areas from 2005 to 2011 provided a unique opportunity for the detailed sampling and study of various components of the deposits in the area. This paper describes various minerals of the Fe-Co-Ni-As-S system and their paragenesis with common ore minerals of the Port Radium deposit. In addition, micro-analytical data and compositional variation in individual minerals are presented, which add some extra light to the complicated mineralogy of the Fe-Co-Ni-As-S mineralization type globally. Furthermore, three unique minerals are introduced. The outcome of this research will not only help to understand the complicated mineralogy of the Port Radium vein-type mineralization but also may assist in defining tools to facilitate exploration of similar deposits in the region and worldwide.

2. Geological Background

The Great Bear magmatic zone is the result of a 1.87–1.85 Ga continental-scale felsic-intermediate Andean-type calc-alkaline magmatism in a continental magmatic arc tectonic setting near the western margin of the Archean Slave craton in northwestern Canada [14,15,18,29–31]. This magmatic arc was formed by eastward subduction-related magmatism following the accretion of the 2.10–1.90 Ga arc-related Hottah terrane to the west and the pre-Great Bear Calderian accretionary wedge and the Slave craton to the east. The products of such extensive magmatism are widespread dacite-rhyodacite-andesite volcanic and volcanoclastic sequences (~1.87 Ga around Port Radium; 14–15, 27) that have been intruded by granite, granodiorite, monzonite, quartz monzonite, and quartz diorite plutons [15,20,24]. This geological setting has provided suitable conditions for the development of regional metasomatic iron and alkalic-calcic (MIAC) mineral systems with iron oxide and alkali-calcic alteration facies and associated critical and precious metal deposits and prospects at 1.87 Ga across the Port Radium–Echo Bay district [18–25,32–37]. The MIAC systems host a few well-known Canadian IOCG and affiliated deposits such as the NICO Au-Co-Bi-Cu and the Sue-Dianne Cu-Ag-Au deposits in the southern GBMZ, and the Mag Hill Co-Ni-U and Port Radium Ni-Co-U-Ag (also named Eldorado mine) vein-type mineralization in the northern GBMZ that are hosted within iron oxide-apatite- and epithermal-type mineralization [20,38]. Some of the deposits in the area have been classified as five-element (Ni-Co-As-Ag-Bi) veins [39]. These younger veins [27] are considered part of the shallow-level epithermal mineralization at Port Radium and Mag Hill [38].

At Port Radium, the intrusion of quartz diorite, quartz monzonite and granite of the Mystery Island plutonic suit into the Echo Bay and Port Radium formations of the Labine Group was coeval with a regional metasomatic system that preferentially replaced, veined, and brecciated the volcanoclastic tuff, volcanic lavas (dacite, rhyodacite and andesite composition), graywacke, and siltstone (Figure 1). The present mineralization comprises early IOCG mineral assemblages overprinted by subsequent epithermal and later-stage veining. The Port Radium–Echo Bay district hosts historical Port Radium, Echo Bay, Bonanza, and El Bonanza U-Ag-Cu ± Ra ± Ni ± Co ± Bi mines, which yielded >5100 tons Cu, >6200 tons U, and >907 tons Ag [20]. The maximum concentration for some metals in drill cores includes 9.47% Cu, 3.81% Pb, 2.93% Zn, 0.84% Ni, 2.50% Co, 1.20% U, 1.7% Bi, 2.3 ppm Au, 206 ppm Ag, and 46 ppm Th (Somarin and Mumin, 2014). Among the

Port Radium/Eldorado vein system (#1 to #9), 89% of the total 0.9 Mt of ore produced was extracted from the veins #1, 2, and 3 [40] studied herein.
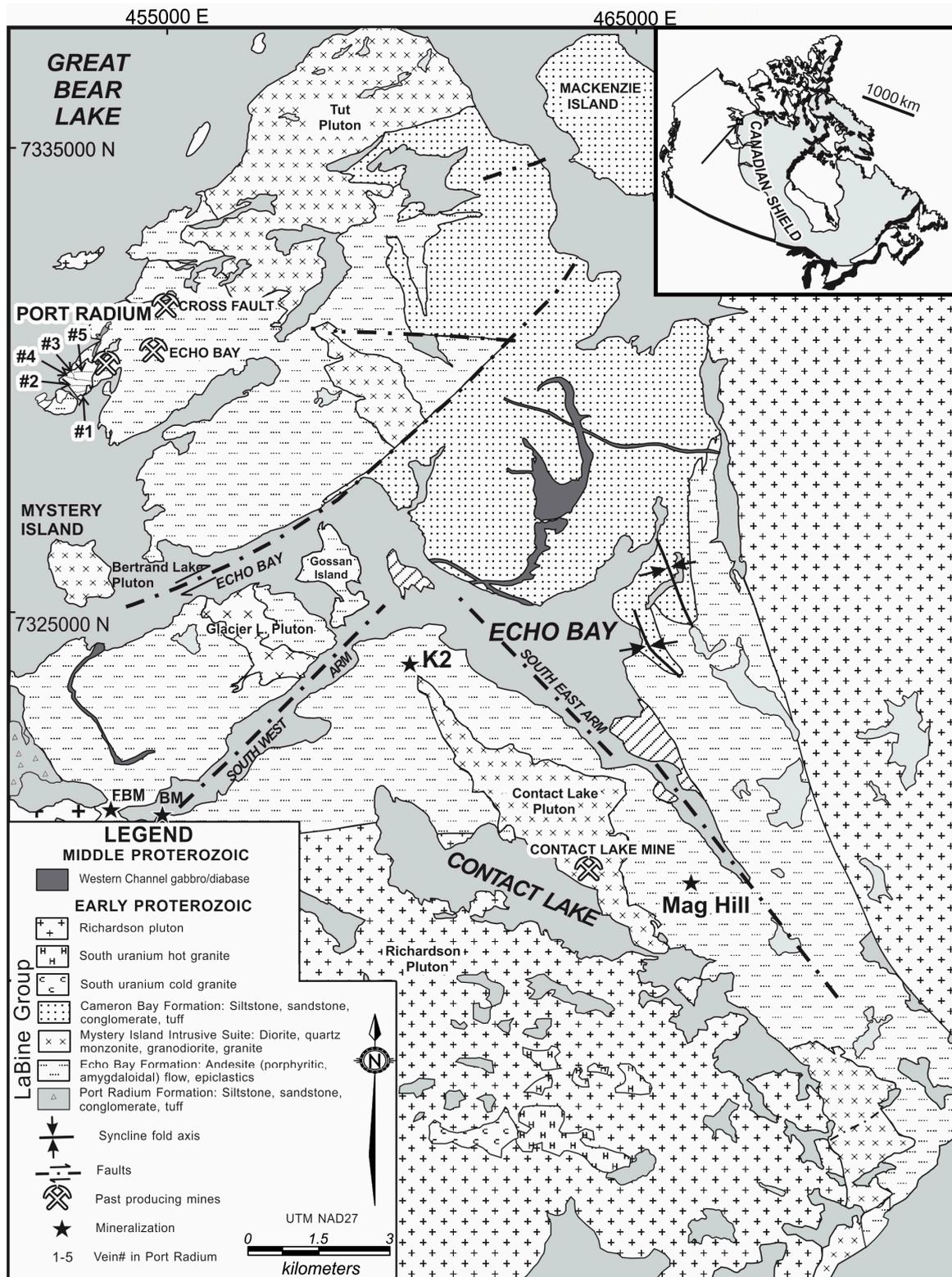

Figure 1. Regional geology map of the GBMZ (modified after [38]). The Port Radium samples were collected from surface and drill cores of hydrothermal veins (#1 to 5). Locations of other deposits (K2, EBM, and Mag Hill) are also shown.

3. Materials and Methods

3.1. Sample Collection and Preparation

More than 200 samples were collected from surface and drill cores of hydrothermal veins (#1 to 5 in Figure 1) and surrounding altered rocks during field mapping and logging of the cores at Port Radium. These samples are distinct from the samples of the Kidd and Haycock (1935) [41] Eldorado Mine collection (stored at the Geological Survey of Canada in Ottawa) that were used by Gandhi et al. (2018) [27].

The drill core samples were cut along the center and varied in length from 20 to 50 cm. The surface samples were 1–3 kg in weight. After visual examination and petrological investigations using hand lenses and stereo microscopes, 50 polished thin sections were made from samples representative of various hydrothermal alteration styles and ore mineral assemblages; these sections were studied using optical microscopy at Brandon University, Canada.

3.2. Analytical Method

Ten polished thin sections with typical ore minerals were selected for further microanalytical investigations using a JEOL JSM-6390LV scanning electron microscope (JEOL USA, Inc., Peabody, MA, USA) equipped with an Oxford Ultim Max 100 SDD energy dispersive spectrometer with an acceleration voltage of 20 kV and a beam current of ~20 nA at Brandon University, Canada. The sections were carbon coated (6 nm thick). The resolution was 5 nm at a working distance of 10 mm. The nominal electron beam diameter was ~2 μm, the nominal detector resolution was ~127 eV, the signal strength in counts per second was ~50,000, and the overall number of counts collected per spectrum was 300,000. The detection limit for all elements varied between 0.2% and 0.35% (Supplementary Table). Analytical uncertainty was ≤0.3 wt%. The analytical data of points with overlapped beams were discarded. Assays with the sum of 97%–102% (lower for hydrous minerals) were used for formula calculations. The standards used for quantification can be found in the Supplementary table.

For the verification and identification of some minerals, three polymetallic samples were selected for X-ray diffractometry (XRD) at Brandon University. The samples were reduced to <75 μm by crushing using a mortar and pestle and passing through a 200-mesh sieve. Five hundred milligrams of each powdered sample were inserted into a 0.5 mm deep steel disc holder with a diameter of 2.5 cm and analyzed. Continuous scan X-ray powder diffraction data were collected over a range of 3–90° 2θ (step size of 0.01°) with CoKa radiation on a Rigaku Miniflex 6 diffractometer (Rigaku Company, Tokyo, Japan)) equipped with a D/tex Ultra2 detector. The fine-focus Co X-ray tube was operated at 40 kV and 0.15 mA, with a scan rate of 10°/min. The X-ray diffractograms were analyzed using Smartlab Studio Version 2 and the American Mineralogist Crystal Structure Database. The Whole Powder Pattern Fitting (Rietveld Refinement) method was used to further refine results and show the semi-quantitative concentration of the minerals present; the detection limit was ~2 vol%.

4. Results

4.1. Hydrothermal Alteration Zones

The hydrothermal alteration zone at Port Radium covers ~10 km^2 and extends eastward and westward across a more than 35 km long MIAC system footprint [26]. Drilling and drill core logging indicates that this zone extends several hundreds of meters at depth while geophysical modeling indicates the system reaches a maximum of about 8 km depth [42,43]. The hydrothermal alteration zones are induced by the staged evolution of the MIAC system into distinct alteration facies [26,33]. From depth at the roof of the sub-volcanic intrusions toward the epithermal cap at the surface, mineral assemblages, hence, facies, vary from the deeper albitite to the subsequent and stratigraphically generally higher magnetite-actinolite-apatite alteration to the potassic-iron and the potassic ± albitic, phyllic, and peripheral/overprinted propylitic alteration types (Figure 2). This alteration

pattern is similar to other deposits in the area (e.g., Mag Hill, K2; Figure 1) and shows a decrease in temperature from depth to surface and toward the peripheral zones. For example, at Mag Hill (~20 km SW of Port Radium), the temperature of the hydrothermal system changed from ~550 °C in the center to <150 °C in the peripheral zones [38]. Tectonic tilting and erosion have partially exposed the albitic root of the system in both Port Radium and Mag Hill. Because of the high magnetite content of the magnetite-actinolite-apatite alteration zone, these deposits can be easily explored using an airborne magnetic anomaly map (Figure 3) [42–44].
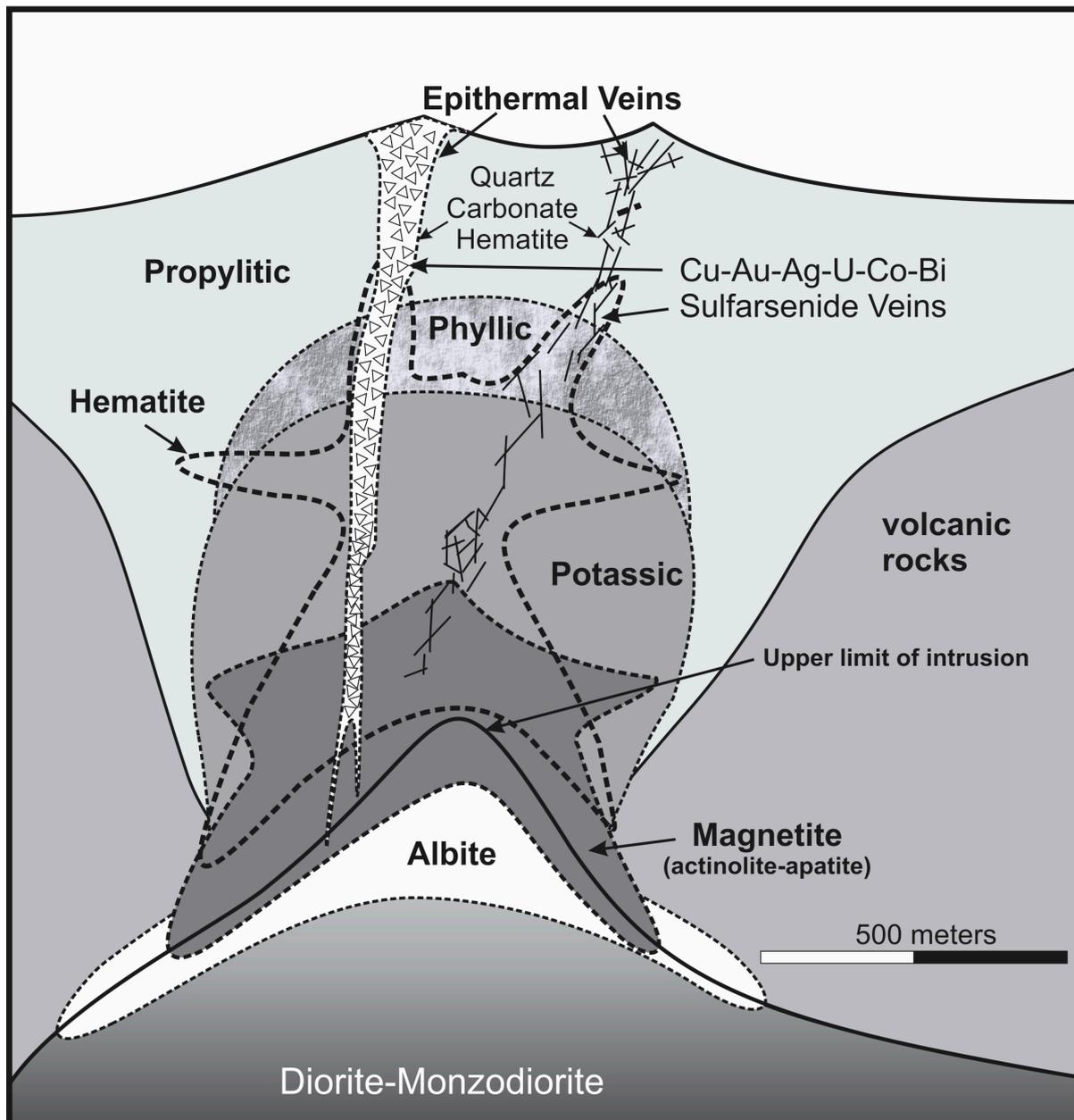
Figure 2. Schematic model showing the spatial relationships of various alteration and mineralization zones at Port Radium (modified after [20]).

Albitization is most intense adjacent to the sub-volcanic intrusions but is common at milder intensity upwardly throughout the region. At Port Radium, albitic alteration occurs as overgrowth of the primary igneous plagioclase in the host volcanic rocks as well as within the groundmass; the only sulfide mineralization at this stage is scarce

disseminated pyrite. Some hydrothermal albite formed later with K-feldspar as veins during potassic ± albitic alteration. The magnetite-actinolite-apatite alteration is found at the surface (Figure 4a) and depth down to several hundreds of meters (Figure 4b). It includes coarse grains of magnetite, dark green actinolite, and pink apatite up to several cm, each grain with a trace amount of pyrrhotite as disseminated grains and open space filling in the volcanic host rocks (Figure 4c). Biotite ± fluorite locally accompanies magnetite-actinolite-apatite alteration (Figure 4d); biotite appears as unaltered booklets and aggregates up to a few centimeters in size; pink fluorite rarely occurs in surface samples. Textural relationships suggest that pyrrhotite formed during and after magnetite mineralization. As the hydrothermal system evolved, the magnetite content of the magnetite-actinolite-apatite alteration was reduced, and it was gradually changed to actinolite-apatite with weak, mainly overprinted pyrrhotite-chalcopyrite-pyrite mineralization.
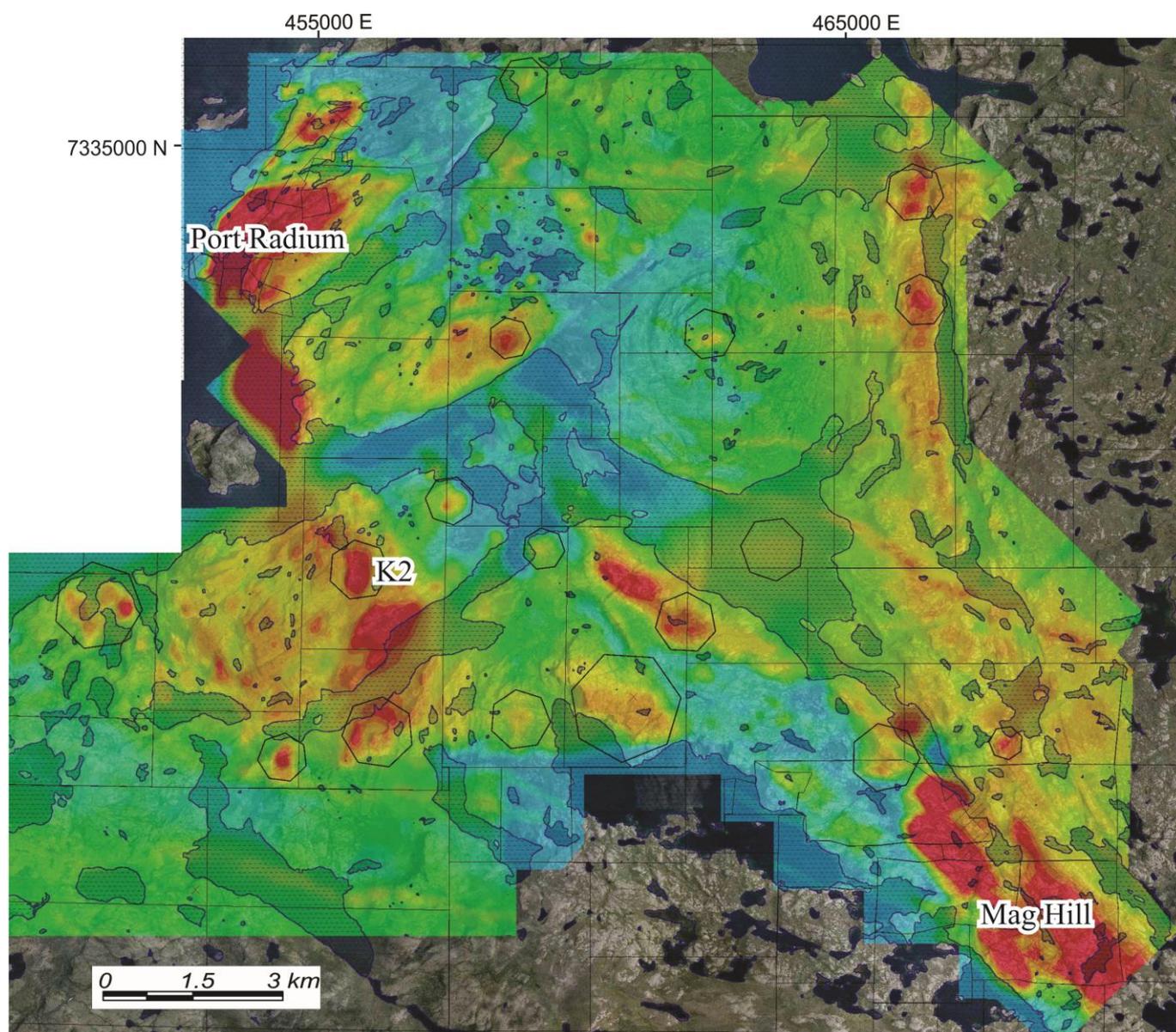
Figure 3. Airborne magnetic anomalies (positive in red; negative in blue) in the Port Radium region. The positive anomalies correspond to magnetite-actinolite-apatite zones in the region.
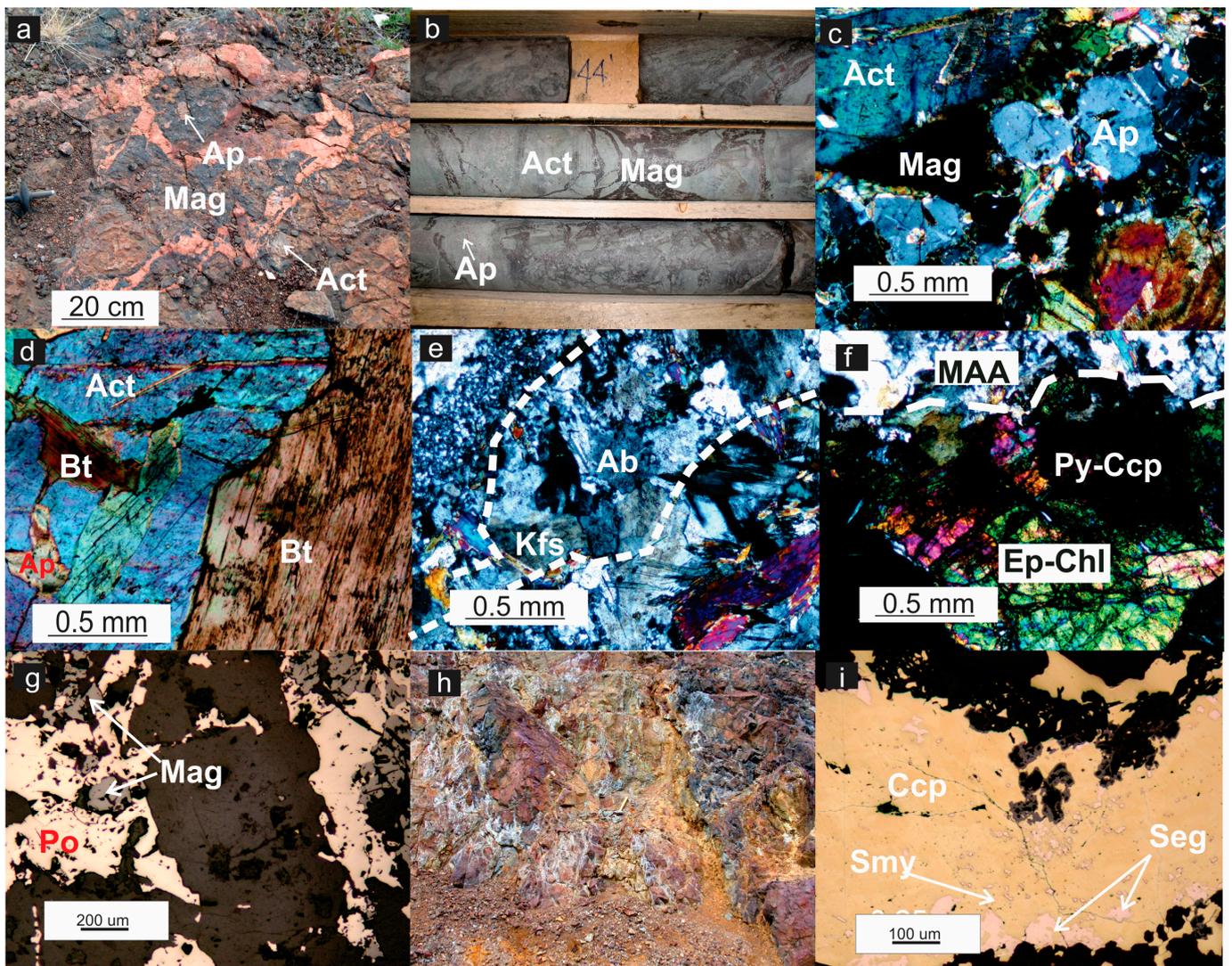
Figure 4. Magnetite-actinolite-apatite-K-feldspar (MAA) assemblage at the surface within a breccia (**a**), in drill core (**b**), and under crossed polarized light (**c**). (**d**) Biotite in contact with and filling fractures in actinolite. (**e**) Albite-K-feldspar veinlet cutting magnetite-actinolite-apatite-feldspar assemblage. (**f**) Epidote-chlorite-pyrite-chalcopyrite vein cutting magnetite-actinolite-apatite-feldspar assemblage. (**g**) Pyrrhotite and magnetite in magnetite-actinolite-apatite zone. (**h**) Strong brecciation along vein #1, where brecciation intensifies toward the vein. (**i**) Siegenite brecciated and hosted by chalcopyrite. Stromeyerite inclusions are disseminated inside chalcopyrite. Abbreviations in Table 1.

Following actinolite-apatite alteration, the potassic ± albitic alteration occurred, which is commonly found at depths > 150 m (Figure 2). It formed K-feldspar ± albite-bearing veins, veinlets, and patchy pink color masses (Figure 4e). In the potassic-altered rocks, K-feldspar occurs as open space filling as well as overgrowth of igneous K-feldspar in the andesitic wall rock. Hydrothermal albite commonly occurs as fine grains (<0.5 mm) in the groundmass of the altered rocks. These albite grains are commonly replaced partially by K-feldspar, suggesting that sodic alteration occurred before potassic alteration. However, albite-bearing potassic veins suggest that some albite formed during this stage as well.

Quartz, sericite, and pyrite are the main products of the phyllic alteration, which occurs sporadically in the andesitic volcanic rocks as moving away from the central part of the Port Radium hydrothermal system (Figure 2). The replacement of igneous feldspars by sericite and overgrowth of igneous quartz are common in phyllic-altered rocks. Compared to the previous alterations, more sulfide minerals (pyrite, chalcopyrite, sphalerite, and

galena) formed at this stage (Figure 5). Phyllic alteration was followed by the propylitic alteration, which formed quartz, chlorite, epidote, carbonate (dolomite, calcite, and scarce siderite) with trace sericite and pyrite ± chalcopyrite ± sphalerite. As noted by Bailey (2017) [45], the carbonate phases in this system are extremely variable in both textures and compositions. The propylitic mineral assemblage occurs as a replacement, open space filling, veins, and veinlets. Replacement of hydrothermal biotite and actinolite by chlorite and plagioclase by epidote are found locally. At depth, propylitic alteration is structurally controlled and mostly occurs as quartz-chlorite ± epidote ± sulfides veins cutting actinolite-apatite and potassic alteration zones (Figure 4f). The propylitic alteration cuts and overlaps previous alterations and extends several kilometers away from the center of the hydrothermal system (Figure 2). Replacement textures and cross-cutting relationships show that propylitic occurred as the last alteration at Port Radium.
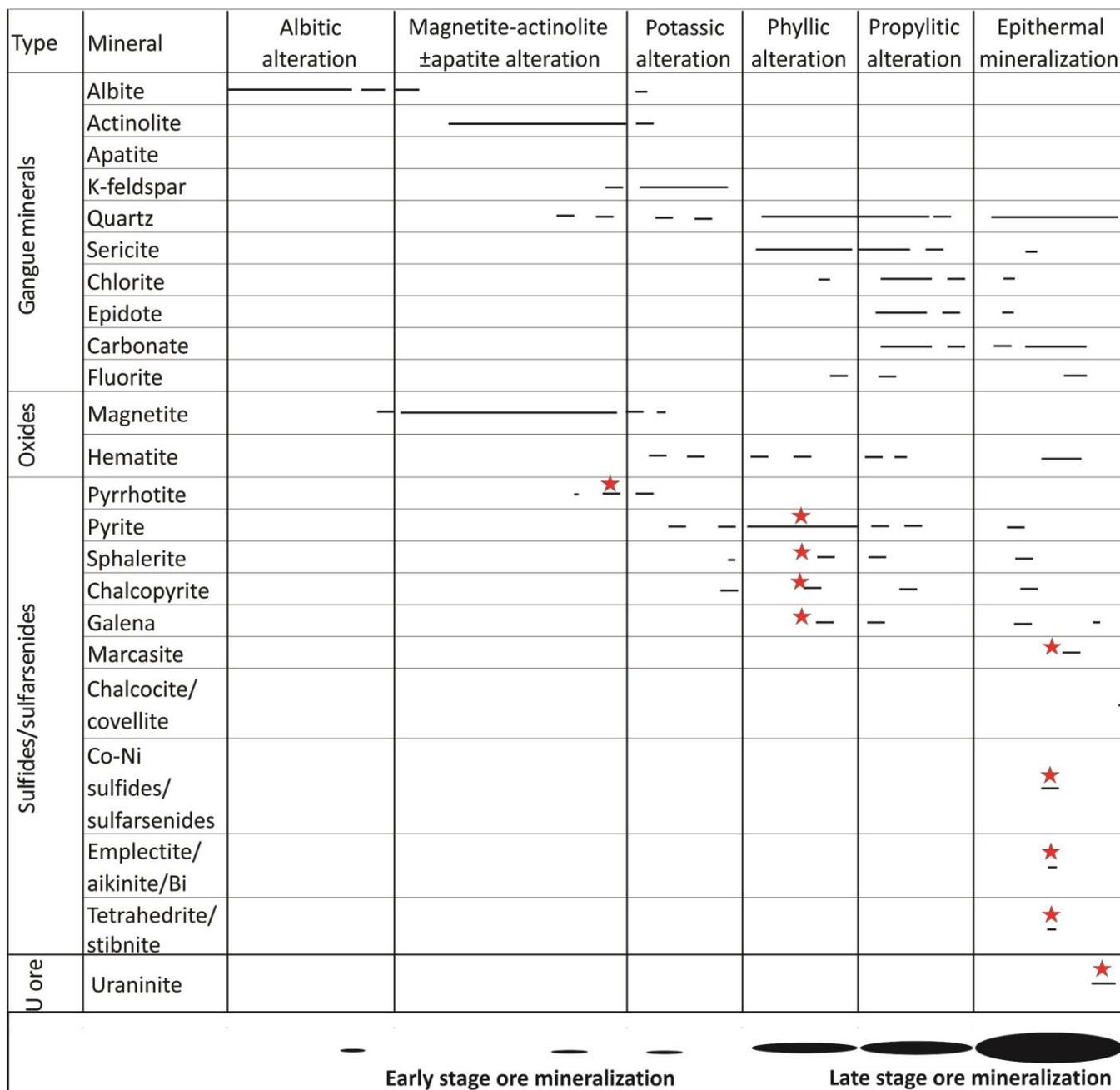

Figure 5. Paragenesis of ore and gangue minerals of Port Radium. Minerals from specific mineralization stages that were analyzed in this study are shown with red stars.

4.2. Ore Mineralization

Based on timing, intensity, and extension, the Port Radium ore mineralization can be subdivided into two stages: (1) early-stage trace mineralization and (2) late-stage major and extensive mineralization. Various ore minerals have formed during these stages (Table 1); the temporal sequence of ore formation is depicted in Figure 5. Fluid inclusion studies [46] show that the early-stage mineralization and magnetite-actinolite-apatite alteration started from high temperature (>500 °C) and high–mid salinity (35–10 wt% NaCl equi.). However, the late-stage minerals precipitated at T < 280 °C from a lower salinity (~5 wt% NaCl equi.) solution. These data are similar to those from the nearby Mag Hill deposit [38], where the late-stage minerals were deposited at a depth of <200 m. Such a shallow depth is also considered for the Port Radium late-stage mineralization.

Table 1. Ore and gangue minerals identified in samples from Port Radium with their acronyms (after [47], except the acronyms marked by star) and nominal compositions.

Mineral	Acronym	Formula	Mineral	Abbreviation	Formula
Actinolite	Act	$Ca_2(Mg_{4.5-2.5}Fe_{0.5-2.5})Si_8O_{22}(OH)_2$	Heterogenite	* Htg	$CoO(OH)$
Aikinite	* Akt	$PbCuBiS_3$	K-feldspar	Kfs	$KAlSi_3O_8$
Albite	Ab	$NaAlSi_3O_8$	Magnetite	Mag	Fe_3O_4
Apatite	Ap	$Ca_5(PO_4)_3(Cl/F/OH)$	Marcasite	Mrc	FeS_2
Arsenopyrite	Apy	$FeAsS$	Niccolite	* Nc	$NiAs$
Biotite	Bt	$K(Fe^{2+}/Mg)_2(Al/Fe^{3+}/Mg/Ti)([Si/Al/Fe]_2Si_2O_{10})(OH/F)_2$	Pyrite	Py	FeS_2
Bismuth	Bi	Bi	Pyrrhotite	Po	FeS
Calcite	Cal	$CaCO_3$	Quartz	Qz	SiO_2
Chalcocite	Cct	Cu_2S	Rammelsbergite	* Rmb	$NiAs_2$
Chalcopyrite	Ccp	$CuFeS_2$	Safflorite (and clinosafflorite)	* Saf	$(Co_{0.8}Ni_{0.2})As_2$ (and $CoAs_2$)
Chlorite	Chl	$(Mg,Fe^{2+},Fe^{3+},Mn,Al)_{12}[(Si,Al)_8O_{20}](OH)_{16}$	Sericite	Ser	$KAl_2(AlSi_3O_{10})(OH)_2$
Cobaltite	* Cbt	$(Co,Fe)AsS$	Siegenite	* Seg	$(Ni,Co)_3S_4$
Coffinite	* Cof	$UO_2.nH_2O$	Skuterrudite	* Skt	$(Co,Fe,Ni)As_{2-3}$
Covellite	Cv	CuS	Sphalertite	Sp	ZnS
Dolomite	Dol	$CaMg(CO_3)_2$	Stibnite	* Stb	Sb_2S_3
Emplectite	* Emp	$CuBiS_2$	Stromeyerite	* Smy	$AgCuS$
Epidote	Ep	$(CaCa)(AlAlFe^{3+})O[Si_2O_7][SiO_4](OH)$	Tetrahedrite	Ttr	$(Cu,Fe,Ag,Zn)_{12}Sb_4S_{13}$
Erythrite	* Ery	$Co_3(AsO_4)_2 \cdot 8H_2O$	Mineral X1	X1	$(Co_{0.96}Ni_{0.45}Fe_{0.03})S_{0.27}As_4$
Fluorite	Fl	CaF_2	Mineral X2	X2	$(Ni_{2.13}Co_{0.38})S_{0.97}As_4$
Galena	Gn	PbS	Mineral X3	X3	$(Ni_{1.83}Co_{0.83})S_{1.25}As_4$
Gersdorffite	* Gdf	$NiAsS$	Uraninite	Urrn	UO_2
Hematite	Hem	Fe_2O_3	Uranophane	* Urf	$Ca(UO_2)2SiO_3(OH)_2.5(H_2O)$

4.2.1. Early-Stage Ore Mineralization

Although albitic, magnetite-actinolite-apatite, and potassic alteration types are intensive, widespread, and show zonal distribution (Figure 2), only scarce pyrrhotite, pyrite, chalcopyrite, and sphalerite formed during these stages of hydrothermal activity in the region (Figure 5). Textural relationships suggest that pyrrhotite formed during and after magnetite mineralization in the magnetite-actinolite-apatite alteration zone (Figure 4g). However, most of the pyrrhotite formed during the actinolite-apatite alteration; the large pyrrhotite grains enclose euhedral apatite crystals with poikilitic texture. In addition, trace sulfide mineralization occurred at this stage and formed chalcopyrite and sphalerite as irregular aggregates, <2 mm in size, accompanied by euhedral to subhedral pyrite grains. Textural and crosscutting relationships indicate that chalcopyrite, sphalerite, and pyrite precipitation was mainly post-pyrrhotite mineralization. This is typical of the high-temperature and low-temperature K-Fe alteration facies [33].

Common opaque minerals in the potassic zone include disseminated scarce magnetite, hematite, pyrrhotite, and pyrite. Spatially and temporally, the magnetite gradually disappeared as the system progressed toward phyllic and propylitic alterations, during which oxide mineralization continued as sporadic hematite and specularite. This is another

characteristic of the low-temperature K-Fe alteration facies in the region [33]. The phyllic and propylitic alterations mark the start of the main sulfide mineralization at Port Radium, which continued later as sulfide-sulfarsenide ± uraninite epithermal mineralization.

4.2.2. Late-Stage Ore Mineralization

The main sulfide mineralization started during the phyllic alteration stage and formed zones with sericite and high sulfide contents (locally visible as gossan at the surface; Figure 4h). Sulfides occur as veinlets, veins, and masses up to several tens of centimeters wide and a few meters long. Pyrite is the most common sulfide in these zones. Pyrite and siegenite occur as skeletal and brecciated grains (Figure 4i) up to 0.5 mm in size, hosted by chalcopyrite; brecciated pyrite grains are also cemented by chalcopyrite. Stromeyerite is rare and occurs as subhedral grains up to 15 microns associated with siegenite, and both are hosted by chalcopyrite (Figure 4i). Stromeyerite is closely associated with an Ag-Se-Te mineral, which occurs as 5–20 micron size inclusions in chalcopyrite.

The sulfide mineralization continued as pyrite-chalcopyrite ± sphalerite ± galena ± marcasite in the quartz–chlorite ± epidote veins. These minerals commonly fill fractures and open spaces in the older magnetite-actinolite-apatite and potassic assemblages. These veins mostly occur close to the surface; however, they are still found sporadically at a depth of ~350 m in drill cores. Pyrrhotite from the previous sulfide mineralization, i.e., during magnetite-actinolite-apatite and potassic alterations (Figure 5), can be found as anhedral to subhedral grains up to 4 mm in size and locally replaced by marcasite. Pyrite occurs as anhedral grains and masses up to 2.5 cm long. Chalcopyrite occurs as inclusions and fills fractures in pyrite. Sphalerite with or without chalcopyrite inclusions is found as masses accompanied by trace galena. At shallow depths where propylitic alteration overprints potassic zone, magnetite and hematite have been obliterated, whereas sulfide mineralization is enhanced locally as pyrite overgrowth and skeletal grains with trace chalcopyrite, sphalerite, galena, and pyrrhotite inclusions.

The main ore mineralization occurred as epithermal-type veins at Port Radium (Figure 5). This mineralization formed five main ore-bearing veins with variable thickness (0.3–3 m) and several hundreds of meters long (Figures 1 and 6a). The mineral assemblages in the veins are variable. These veins are W-NW striking with a near vertical dip that shows evidence of multiple hydrothermal events during episodic shearing and fracturing, which extend 0.2–1 m into their immediate wall rocks (Figures 4h and 6a). The cement of the breccia is mainly composed of quartz ± dolomite ± calcite, which occur as subhedral to euhedral grains with local growth zoning; the wall rock fragments in the breccia commonly show hydrothermal alteration, particularly propylitic assemblages. Uranium mineralization is mainly associated with the polymetallic sulfide and sulfarsenide veins that were historically mined for U, Cu, and Ag at Port Radium. It is notable that not all sulfide and sulfarsenide veins have uraninite.

Various assemblages of the epithermal stage are described below.

Epithermal Sulfide Assemblages

Quartz-Pyrite-Chalcopyrite Vein

This vein cuts the brecciated chlorite-sericite (propylitic) altered ash tuff and greywacke that are cemented by quartz. Sulfides are mainly in the vein, but traces are also found as disseminated grains and veinlets in the wall rocks. Chalcopyrite occurs as masses up to several centimeters, accompanied by subhedral to euhedral pyrite grains up to 2 mm in size, trace sphalerite, and supergene chalcocite and covellite.

Quartz-Carbonate-Epidote-Chlorite-Pyrite-Chalcopyrite-Galena-Sphalerite Assemblage

This assemblage occurs as irregular masses and veins up to a few cm thick and 1 m long. Locally, anhedral to subhedral grains of epidote up to 1 cm in size comprise 85 vol% of the veins. Adularia occurs sporadically along the vein walls and infiltrates into the host rock. Galena occurs as individual grains associated with chalcopyrite or as a replacement for pyrite. Marcasite is common and replaces pyrrhotite and pyrite.

Commonly, galena, sphalerite, and chalcopyrite fill fractures in pyrite. Some sphalerite grains host chalcopyrite inclusions: based on optical features, most sphalerite grains are Fe-poor. Locally, chalcopyrite is rimmed by galena, which itself is rimmed by sphalerite, indicating that chalcopyrite is paragenetically older. Sphalerite $\pm$ galena $\pm$ chalcopyrite infill fractures and replace pyrrhotite and pyrite, indicating that pyrrhotite $\pm$ pyrite (formed during magnetite-actinolite-apatite alteration) are the oldest sulfides at Port Radium. This agrees with a general paragenetic sequence of the Port Radium deposit, which is similar to that at Mag Hill [38].
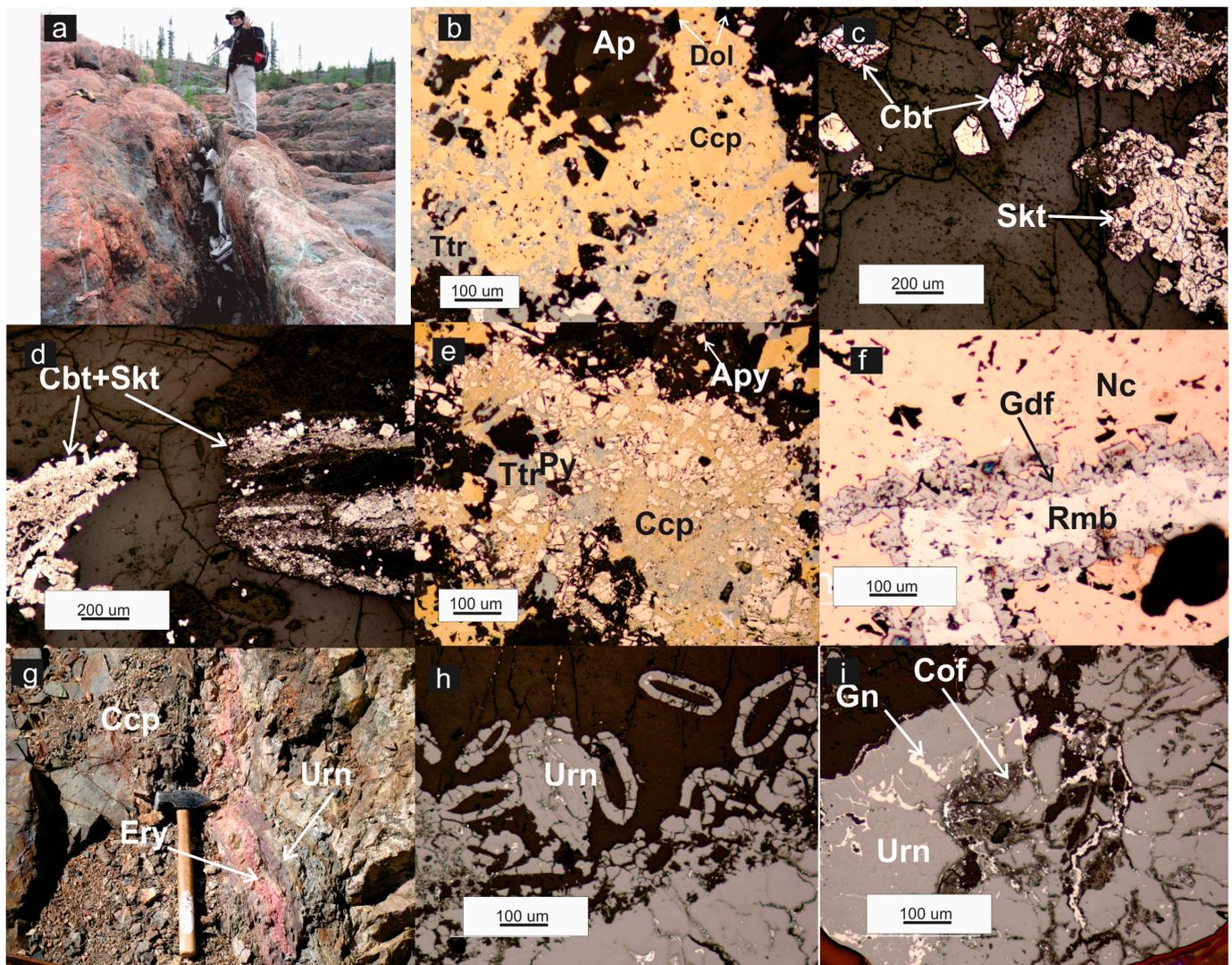
Figure 6. (**a**) Vein #4, which is similar to other veins, has variable thickness with brecciated wall rock. (**b**) Apatite from magnetite-actinolite-apatite assemblage overprinted by epithermal minerals, including chalcopyrite hosting euhedral dolomite and arsenopyrite, fine anhedral pyrite and tetrahedrite. (**c**) Subhedral to euhedral cobaltite accompanied by zoned skutterudite. (**d**) Fine-grained cobaltite and skutterudite in the brecciated wall rock fragments (right side), along with coarse-grained open space filling cobaltite-skutterudite in the vein (left side). (**e**) Subhedral to anhedral pyrite grains brecciated and cemented by chalcopyrite and arsenobismuthian tetrahedrite. (**f**) Nickeline cut by a veinlet of rammelsbergite; gersdorffite occurs between these two minerals. (**g**) Sulfarsenide-uraninite vein #3: occurrence of uraninite in the center of the vein is notable. (**h**) Colloform uraninite with quartz nucleus. (**i**) Galena and trace coffinite as decay and alteration products of uraninite, respectively. Abbreviations in Table 1.

Epithermal Sulfarsenide Assemblages

Quartz-Carbonate-Cobaltite-Skutterudite-Pyrite-Chalcopyrite ± Sphalerite ± Arsenopyrite Assemblage

This assemblage is a part of vein #3 at Port Radium. The exposed part of the vein is 0.2–1.5 m wide and several hundred meters long. The andesitic wall rock that is cut by the vein shows phyllic alteration, and it is brecciated near the vein wall. Quartz and euhedral dolomite occur as coarse grains up to 6 mm (Figure 6b). Cobaltite occurs as subhedral to euhedral grains up to 1 mm in size, accompanied by zoned skutterudite up to 3 mm in size (Figure 6c). Two types of cobalt mineralization are found in this vein: (1) cobaltite-skutterudite in the intensely altered and brecciated wall rock fragments that are cemented by quartz-calcite-siderite; (2) cobaltite-skutterudite as coarser grains filling open spaces in the vein (Figure 6d).

A similar assemblage also occurs as part of vein #1 that cuts intensely brecciated Port Radium Formation (Figure 4h) with chlorite-carbonate (propylitic) alteration. In this vein, chalcopyrite occurs as massive aggregates up to a few 10 s cm in size, containing inclusions of other sulfides. Millimeter to centimeter-scale sphalerite with or without chalcopyrite inclusions accompanies chalcopyrite masses. Arsenopyrite, as <2 mm euhedral grains, fills spaces between chalcopyrite and sphalerite grains or occurs as inclusions inside them. Subhedral to anhedral pyrite grains < 3 mm in size have been brecciated and cemented by chalcopyrite and arsenobismuthian tetrahedrite (Figure 6e).

Quartz-Nickeline-Cobaltite-Rammelsbergite-Gersdorffite Assemblage

This assemblage is a part of vein #1 and represents Ni-Co arsenide mineralization at Port Radium. Both nickeline and rammelsbergite are the main arsenides associated with cobaltite and form masses up to a few tens of centimeters. Rammelsbergite fills fractures in nickeline. Gersdorffite occurs as subhedral grains along the contact of nickeline and rammelsbergite (Figure 6f). It appears that gersdorffite is the reaction product of rammelsbergite with an S-bearing solution. These relationships suggest that nickeline and cobaltite form contemporaneously, followed by rammelsbergite and gersdorffite.

Uranium-Sulfide-Sulfarsenide Assemblages

Quartz-Uraninite-Pyrite-Chalcopyrite ± Cobaltite ± Arsenopyrite ± Tetrahedrite ± Galena Assemblage

This assemblage is a part of vein #1, which was one of the main veins mined at Port Radium. Although this vein has a polymetallic assemblage, not all ore minerals have formed at the same time; occurrence of uraninite in the center of the vein (Figure 6g) and cutting of quartz-pyrite-chalcopyrite ± cobaltite ± arsenopyrite ± tetrahedrite ± galena assemblage by quartz-uraninite veinlets suggest that uranium mineralization occurred after sulfarsenide crystallization in the same vein (Figure 5).

In the center of the vein, quartz occurs as anhedral to subhedral grains up to 1.2 cm long. Uraninite is the main ore mineral in the vein center and occurs as colloform and botryoidal masses up to a few centimeters in size. Some colloform uraninite masses have quartz as nucleolus (Figure 6h). Galena and trace coffinite as decay and alteration products of uraninite, respectively, accompany and fill fractures in uraninite (Figures 6i and 7). Trace stibnite was also found in the XRD analysis (Figure 7). Uranophane is found in the weathered samples.

In the quartz-pyrite-chalcopyrite ± cobaltite ± arsenopyrite ± tetrahedrite ± galena veinlets, all sulfides are in trace amounts. Cobaltite and arsenopyrite occur as subhedral to euhedral crystals up to 0.5 mm. Tetrahedrite is anhedral, up to 0.25 mm in size, and commonly accompanies chalcopyrite.

Quartz-Carbonate-Pyrite-Chalcopyrite-Cobaltite-Skutterudite-Rammelsbergite-Aikinite-Emplectite-Native Bismuth-Uraninite Assemblage

This assemblage is also part of vein # 1. Although the hand specimen does not contain visible uraninite, U mineralization has been observed in other parts of this vein (Figure 6g). The wall rock shows intense brecciation where chlorite-epidote-carbonate (propylitic)

altered country rocks have been cemented by carbonate. Chalcopyrite and pyrite occur as trace disseminated grains and aggregates up to 5 mm in size, in which chalcopyrite locally fills fractures in pyrite. Aikinite (fine grains were verified by XRD; Figure 7) rims sphalerite and chalcopyrite (Figure 8a), suggesting it formed after base metal sulfides. Also, aikinite occurs as subhedral grains up to 0.3 mm in size associated with native bismuth, emplectite (verified by XRD; Figure 7), and Ni-Co sulfide/sulfarsenides (Figure 8b,c). Cobaltite and skutterudite form rhythmic bands; cobaltite bands have slightly lighter colors compared to the skutterudite bands (Figure 8b). Skutterudite grains up to 3 mm are commonly zoned (Figure 8d). Concentric bands of safflorite + clinosafflorite (differentiated based on their composition) are commonly rimmed by cobaltite and skutterudite (Figure 8e).
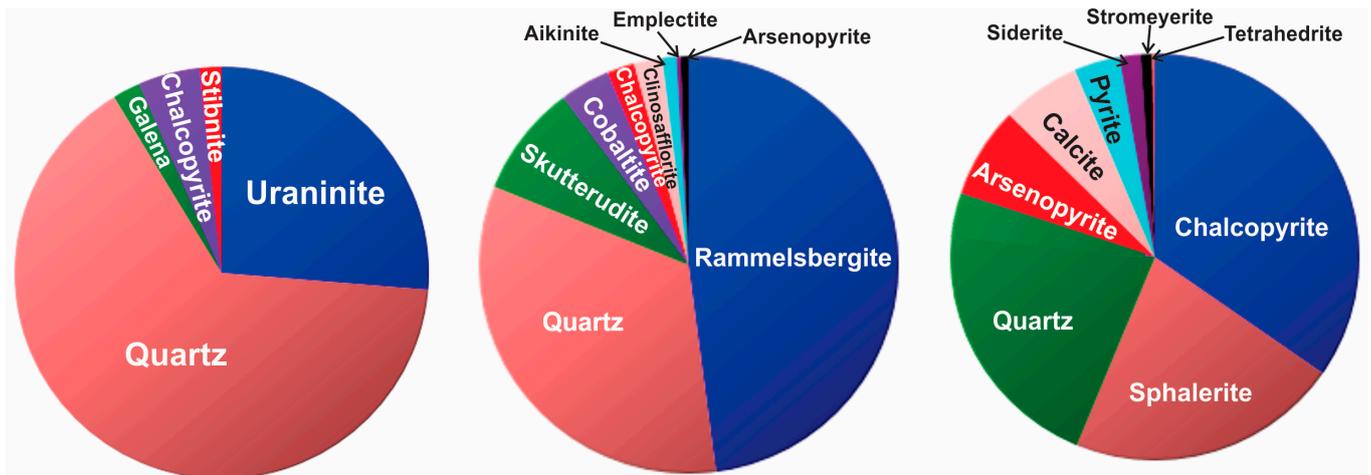
Figure 7. Pie diagrams showing semi-quantitative results of XRD analysis of three representative samples from epithermal sulfide (Figure 6e), arsenide (Figure 6c,d), and uranium-sulfide-sulfarsenide (Figure 6h,i) assemblages.
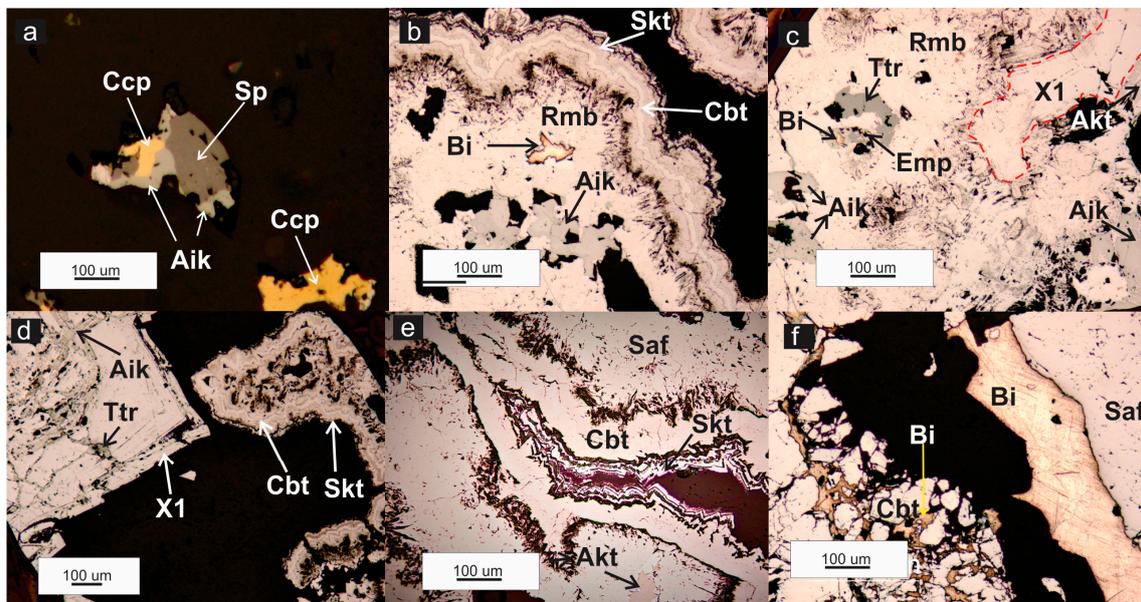
Figure 8. (**a**) Aikinite rims sphalerite and chalcopyrite. (**b**) Spherulitic rammelsbergite with inclusions of native bismuth and aikinite rimmed by cobaltite-skutterudite. (**c**) Rammelsbergite with inclusions of tetrahedrite, aikinite, emplectite, native bismuth, and mineral X1. (**d**) Aikinite filling cracks and growth zones in skutterudite. (**e**) Safflorite rimmed by cobaltite and skutterudite. (**f**) Native bismuth rims safflorite and fills cracks in cobaltite. Abbreviations in Table 1.

There are three unique minerals that are closely associated with other Ni-Co sulfarsenides. The first one (called X1 herein) has the following characteristics: growth zoning, white color with a faint creamy tint in polarized light, without pleochroism, and isotropic or weakly anisotropic (Figure 8c,d). This mineral has optical properties similar to skutterudite; however, its chemistry is different (see below). The second unique mineral (called X2 herein) occurs as concentric bands with creamy white color in polarized light, strong anisotropy, and without pleochroism (Figure 8e). Optically, this mineral is similar to rammelsbergite, but its chemistry is different (see below). The third unique mineral (X3) is less common, closely associated with rammelsbergite, and optically similar to mineral X2. Due to their small size (<0.5 mm), the physical properties of these un-named minerals were not determined. However, it seems that they have a steel grey color with metallic luster (similar to cobaltite) in hand specimen. These minerals were not detected in XRD analysis due to their low concentration (<~2 vol%).

Native bismuth rims safflorite and fills cracks in cobaltite (Figure 8f). Native silver was not found in these samples. Emplectite occurs as fine inclusions up to 50 microns associated with aikinite (Figure 8c). Erythrite and heterogenite are common weathering products of cobaltite (Figure 6g).

In this assemblage, quartz grains are up to 1 cm long with growth zoning. Dolomite occurs as open space filling. Where this vein cuts the magnetite-actinolite-apatite zone, magnetite is hematitized along grain boundaries/margins, and chlorite-calcite-quartz occurs as a pseudomorph after actinolite.

4.3. Mineral Chemistry

Pyrrhotite has up to 0.81% Ni and 0.35% Co (Table 2). Pyrite grains have higher Ni (up to 2.09%) and Co (up to 0.48%) than pyrrhotite. Marcasite has similar Co (up to 0.50%) but more Ni (up to 5.02%) than pyrite (Table 2). These elements are likely substitutes for Fe in the structure of these minerals [48]. Chalcopyrite has up to 0.39% Sb and 0.36% Co (Table 2). Some arsenopyrite grains have traces of Co, Ni, Cu, and Sb (Table 3). The Port Radium arsenopyrite is nearly stoichiometric with a mean composition of $Fe_{1.00}Co_{0.02}As_{0.99}S_{0.98}$.

Emplectite is relatively rare and has up to 0.23% Co, 0.35% Ni, and 0.72% Sb with a near stoichiometric composition of $Cu_{1.01}Bi_{0.99}Sb_{0.01}Ni_{0.01}S_{1.98}$. Aikinite contains up to 0.39% Ag, 0.60% Fe, 0.40% Ni, and 0.31% Co (Table 4) with a stoichiometric composition of $Pb_{0.97}Cu_{0.99}Bi_{0.99}S_{3.02}$.

Most of the microanalysis of stromeyerite did not produce reliable results due to its small size and beam overlap with the host chalcopyrite. However, this mineral was identified in the XRD analysis (Figure 7). One relatively larger grain produced reliable data with 1.02% Fe (Table 5). Stromeyerite is closely associated with an Ag-Se-Te mineral with a tentative formula of $Fe_{0.19}Cu_{0.49}Ag_{3.31}Se_{1.64}S_{0.25}Te_{0.13}$ which could be a Te-bearing aquilarite (Ag_4SeS) or naumannite (Ag_2Se) with some Fe-Cu-S input from the host chalcopyrite. Assuming all Fe, Cu, and S to come from chalcopyrite, the composition of this mineral is calculated to be $Ag_2Se_1Te_{0.08}$ corresponding to a Te-bearing naumannite.

The Port Radium uraninite is characterized by a UO_2 range of 76.77%–86.70% (average 84.18%) and high PbO (9.90%–22.37% with an average of 13.67%) (Table 6). The high Pb content is similar to the Eagle Point, Macarthur River, and Camie River deposits in Canada [49]. The lead has an overall negative correlation with UO_2, showing that it is likely the decay product of uranium (Figure 9a). This may indicate that age was the main factor controlling the Pb content of uraninite; however, the scattering of data suggests that another factor, mainly the degree of alteration, was also an important factor. ZrO_2 reaches up to 2.43% and has preserved its initial substitution trend with uranium (Figure 9b). SiO_2 and FeO are low (average 0.77% and 0.26%, respectively) and show a negative correlation with PbO in uraninite grains that are replaced by coffinite (Figure 9c). Both SiO_2 and FeO are probably hosted by coffinite [45]. There is no chemical difference between colloform and other forms of uraninite. Coffinite composition shows a wider range (Table 6), which depends on the amount of replacement.

Table 2. Representative analyses (in weight%) of pyrrhotite, pyrite, marcasite, and chalcopyrite from the Port Radium deposit.

	Pyrite FeS$_2$								Chalcopyrite CuFeS$_2$			
Sample	114A-PR-1-1	114A-PR-1-2	114A-PR-1-7	114A-PR-0-2	127 PR-1-16	127 PR-2-13	127 PR-2-15	127C PR-1-11	126-PR-1-2	126-PR-2-6	127C-PR-3-10	183C-PR-1-28
S	52.68	52.38	53.00	51.91	52.42	52.68	52.49	53.51	32.64	32.19	36.10	35.08
Fe	45.66	47.38	47.12	46.62	42.63	45.82	42.89	41.14	31.93	32.43	31.04	29.78
Co	0.28	0.34	<0.20	0.48	0.50	<0.20	<0.20	<0.20	<0.20	0.30	<0.20	0.36
Ni	2.09	<0.20	0.87	<0.20	4.45	1.77	4.44	5.02	<0.20	<0.20	<0.20	<0.20
Cu	<0.20	<0.20	<0.20	<0.20	<0.20	<0.20	<0.20	<0.20	35.70	35.33	33.54	34.13
Sb	<0.25	<0.25	<0.25	<0.25	<0.25	<0.25	<0.25	<0.25	<0.25	<0.25	<0.25	0.39
Total	100.70	100.10	100.99	99.02	100.01	100.27	99.82	99.67	100.27	100.24	100.68	99.74
	Number of ions based on 3 atoms								Number of ions based on 4 atoms			
S	1.971	1.970	1.974	1.973	1.976	1.977	1.980	2.010	1.893	1.872	2.038	2.013
Fe	0.981	1.023	1.008	1.017	0.922	0.987	0.929	0.887	1.063	1.083	1.006	0.981
Co	0.006	0.007	0.000	0.010	0.010	0.000	0.000	0.000	0.000	0.009	0.000	0.011
Ni	0.043	0.000	0.018	0.000	0.092	0.036	0.091	0.103	0.000	0.000	0.000	0.000
Cu	0.000	0.000	0.000	0.000	0.000	0.000	0.000	0.000	1.044	1.036	0.956	0.988
Sb	0.000	0.000	0.000	0.000	0.000	0.000	0.000	0.000	0.000	0.000	0.000	0.006

Table 3. Representative analyses (in weight%) of arsenopyrite, sphalerite, and galena from the Port Radium deposit.

	Arsenopyrite FeAsS					Sphalerite ZnS					Galena PbS			
Sample	183A-PR-9	183A-PR-25	183A-PR-26	120 PR-2-17	Sample	127C-PR-1-3	127C-PR-1-10	127C-PR-4-5	127C-PR-4-7	Sample	114A-PR-1-13	114A-PR-1-14	127C-PR-3-3	182B PR-1-2
As	46.71	43.74	46.10	45.61	S	34.39	33.36	33.06	33.11	S	13.59	13.78	12.85	13.56
S	18.42	19.99	18.62	19.84	Fe	2.42	2.89	1.46	0.73	Fe	1.22	1.12	0.00	0.00
Fe	33.90	34.68	34.79	32.73	Ni	<0.20	<0.20	<0.20	<0.20	Cu	<0.20	<0.20	<0.20	0.47
Co	<0.20	<0.20	<0.20	2.23	Cu	1.68	1.87	<0.20	<0.20	Zn	<0.20	<0.20	<0.20	0.41
Ni	<0.20	<0.20	0.28	<0.20	Zn	62.57	62.54	65.14	64.79	Ag	<0.35	<0.35	<0.35	0.64
Cu	0.50	0.41	0.63	<0.20	Total	101.06	100.66	99.66	98.63	Te	<0.35	<0.35	0.41	<0.35
Sb	<0.25	<0.25	<0.25	0.61						Pb	85.23	85.16	86.71	84.97
Total	99.53	98.82	100.43	101.01						Total	100.04	100.06	99.97	100.05

Table 3. *Cont.*

Arsenopyrite FeAsS					Sphalerite ZnS					Galena PbS			
Number of ions based on 3 atoms					Number of ions based on 2 atoms					Number of ions based on 2 atoms			
As	1.032	0.955	1.007	0.984	S	1.022	1.001	1.004	1.014	S	0.989	0.998	0.975	0.992
S	0.951	1.019	0.950	1.000	Fe	0.041	0.050	0.025	0.013	Fe	0.051	0.047	0.000	0.000
Fe	1.005	1.015	1.019	0.947	Ni	0.000	0.000	0.000	0.000	Cu	0.000	0.000	0.000	0.017
Co	0.000	0.000	0.000	0.061	Cu	0.025	0.028	0.000	0.000	Zn	0.000	0.000	0.000	0.015
Ni	0.000	0.000	0.008	0.000	Zn	0.912	0.921	0.970	0.973	Ag	0.000	0.000	0.000	0.014
Cu	0.013	0.011	0.016	0.000						Te	0.000	0.000	0.008	0.000
Sb	0.000	0.000	0.000	0.008						Pb	0.960	0.955	1.018	0.962

Sphalerite grains without chalcopyrite inclusions have a wide range of Cu from below detection limit to 3.19%, whereas Cu range is narrow (0.45%–1.07%) in sphalerite grains with chalcopyrite inclusions. Similarly, chalcopyrite-free sphalerite has wider Fe content (0.58%–4.76%) compared to the chalcopyrite-bearing sphalerite (1.46%–2.23%). Overall, Fe content is low, which reflects light color of the Port Radium sphalerite (Table 3). Galena contains up to 0.64% Ag and 2.7% Zn (Table 3). Native bismuth has traces of As (up to 0.4%) and Ag (0.58% in one sample). The Port Radium tetrahedrite is enriched in As and Bi up to 6.85% and 8.27%, respectively (Table 4), with a mean composition of $(Cu_{9.32}Ag_{0.52})(Zn_{1.28}Fe_{0.77}Ni_{0.03}Co_{0.01})(Sb_{3.22}As_{0.71}Bi_{0.19})S_{12.95}$.

Table 4. Representative analyses (in weight%) of tetrahedrite, emplectite, and aikinite from the Port Radium deposit.

Tetrahedrite $(Cu,Fe,Ag,Zn)_{12}(Sb,Bi,As)_4S_{13}$

Sample	183A-PR-16	183C-PR-1-22	183C-PR-1-23	183A-PR-28
S	24.10	25.07	24.99	23.83
Fe	3.41	1.38	1.69	3.40
Cu	32.53	37.76	38.17	32.42
Zn	4.39	6.32	5.66	4.48
As	1.05	3.76	6.61	<0.20
Ag	6.98	0.52	0.44	6.55
Sb	26.43	21.23	16.69	28.12
Bi	<0.20	4.70	6.28	<0.20
Total	98.90	100.73	100.54	98.79
Number of ions based on 29 atoms				
S	12.917	12.962	12.870	12.872
Fe	1.049	0.410	0.500	1.054
Cu	8.797	9.851	9.918	8.836
Zn	1.154	1.602	1.429	1.187
As	0.241	0.832	1.457	0.000
Ag	1.112	0.080	0.067	1.051
Sb	3.729	2.890	2.263	3.999
Bi	0.000	0.373	0.496	0.000

Emplectite $CuBiS_2$

Sample	183C-PR-1-18	183C-PR-1-19	183C-PR-1-25	183C-PR-3-14
S	18.66	19.52	18.97	18.53
Co	<0.20	<0.20	0.23	<0.20
Ni	<0.20	0.35	<0.20	<0.20
Cu	18.90	19.40	19.90	18.63
As	<0.25	<0.25	<0.25	0.42
Sb	0.56	0.72	0.44	<0.25
Bi	60.51	60.60	60.51	60.87
Total	98.63	100.59	100.06	98.45
Number of ions based on 4 atoms				
S	1.984	2.003	1.969	1.979
Co	0.000	0.000	0.013	0.000
Ni	0.000	0.020	0.000	0.000
Cu	1.014	1.004	1.042	1.004
As	0.000	0.000	0.000	0.019
Sb	0.016	0.019	0.012	0.000
Bi	0.987	0.954	0.964	0.998

Aikinite $PbCuBiS_3$

Sample	183C-PR-1-17	183C-PR-3-10	183C-PR-3-11	183C-PR-4-11
S	16.94	16.85	17.42	16.90
Co	<0.20	<0.20	<0.20	0.31
Cu	11.22	10.91	11.49	11.48
As	<0.25	<0.25	0.40	<0.25
Pb	35.93	34.40	34.18	35.59
Bi	36.65	37.56	37.10	35.38
Total	100.74	99.72	100.59	99.66
Number of ions based on 6 atoms				
S	3.008	3.023	3.041	3.000
Co	0.000	0.000	0.000	0.030
Cu	1.005	0.988	1.012	1.028
As	0.000	0.000	0.030	0.000
Pb	0.987	0.955	0.923	0.978
Bi	0.999	1.034	0.994	0.964

**Table 5.** Composition (in weight%) of stromeyerite and an Ag-Se-Te phase from the Port Radium deposit.

Stromeyerite AgCuS		Ag-Se-Te Phase $Fe_{0.19}Cu_{0.49}Ag_{3.31}Se_{1.64}S_{0.25}Te_{0.13}$	
Sample	126-PR-2-8	Sample	126-PR-2-7
S	24.01	S	1.45
Fe	1.02	Fe	1.95
Cu	45.10	Cu	5.65
Ag	30.23	Ag	65.14
Total	100.36	Se	23.65
		Te	2.99
		Total	100.83
Number of ions based on 3 atoms		Number of ions based on 6 atoms	
S	1.279	S	0.247
Fe	0.031	Fe	0.192
Cu	1.212	Cu	0.487
Ag	0.478	Ag	3.306
		Se	1.640
		Te	0.128

Table 6. Composition (in weight%) of uraninite and coffinite from the Port Radium deposit.

Sample	Uraninite UO_2				Coffinite $UO_2.nH_2O$				Coffinite Replacing Uraninite		
	120 PR-2-1	120 PR-2-4	120 PR-4-2	120 PR-5-1	120 PR-2-9	120 PR-2-16	120 PR-2-10	120 PR-2-11	120 PR-2-7	120 PR-2-8	120 PR-2-6
SiO_2	1.07	0.5	<0.20	<0.20	11.05	15.29	17.17	13.96	6.51	14.30	5.01
FeO	0.71	<0.20	<0.20	<0.20	<0.20	<0.20	0.48	0.32	0.31	0.36	0.52
ZrO_2	2.13	1.72	<0.20	<0.20	2.77	3.09	5.93	4.34	2.34	3.18	3.04
PbO	10.5	13.16	15.58	13	24.68	13.44	5.68	8.31	16.31	17.14	14.24
UO_2	85.51	84.71	84	86.27	47.86	54.32	71.46	73.67	74.55	58.71	72.73
Total	99.92	100.09	99.58	99.27	86.36	86.14	100.72	100.6	100.02	93.69	95.54
	Number of ions based on 2 O						Number of ions based on 4 O				
Si	0.050	0.020	0.030	0.040	0.840	1.040	0.960	0.860	0.500	0.920	0.400
Fe	0.030	0.000	0.000	0.000	0.000	0.000	0.020	0.020	0.020	0.020	0.040
Zr	0.050	0.040	0.000	0.000	0.100	0.100	0.160	0.120	0.080	0.100	0.120
Pb	0.120	0.160	0.210	0.160	0.500	0.060	0.080	0.140	0.340	0.300	0.300
U	0.830	0.860	0.870	0.880	0.800	0.820	0.840	0.940	1.220	0.840	1.300

Fe-Co-Ni-As-S System

The only Ni-Co sulfide found in this research is siegenite, which has up to 0.63% Cu and 4.21% Fe (Table 7) with a mean analytical formula of $Ni_{1.34}Co_{1.64}Fe_{0.12}Cu_{0.01}S_{3.89}$. Nickeline and rammelsbergite have up to 0.82 and 3.04% Co with mean formulas of $Ni_{0.99}As$ and $Ni_{0.95}Co_{0.04}S_{0.08}As_{1.92}$, respectively (Table 7); the latter has also up to 0.31% Sb (Table 7). Gersdorffite (mean formula $Ni_{0.96}Co_{0.02}As_{1.10}S_{0.91}$) generally has <0.5% Co (except in one sample with 3.44% Co; Table 7); one sample has 12.38% Co with a formula of $Ni_{0.60}Co_{0.34}Fe_{0.08}As_{0.93}S_{1.01}$, which is named cobaltoan gersdorffite herein. Common clinosafflorite has up to 1.2% Ni with a mean formula of $Co_{0.89}Ni_{0.02}Fe_{0.08}S_{0.06}As_{1.94}$ (Table 8); however, some safflorite grains have 3.52%–6.14% Ni which yields a mean formula of $Co_{0.74}Ni_{0.18}Fe_{0.10}S_{0.08}As_{1.90}$. Optical properties of nickeliferous safflorite and cobaltoan gersdorffite are the same as safflorite and gersdorffite, respectively.
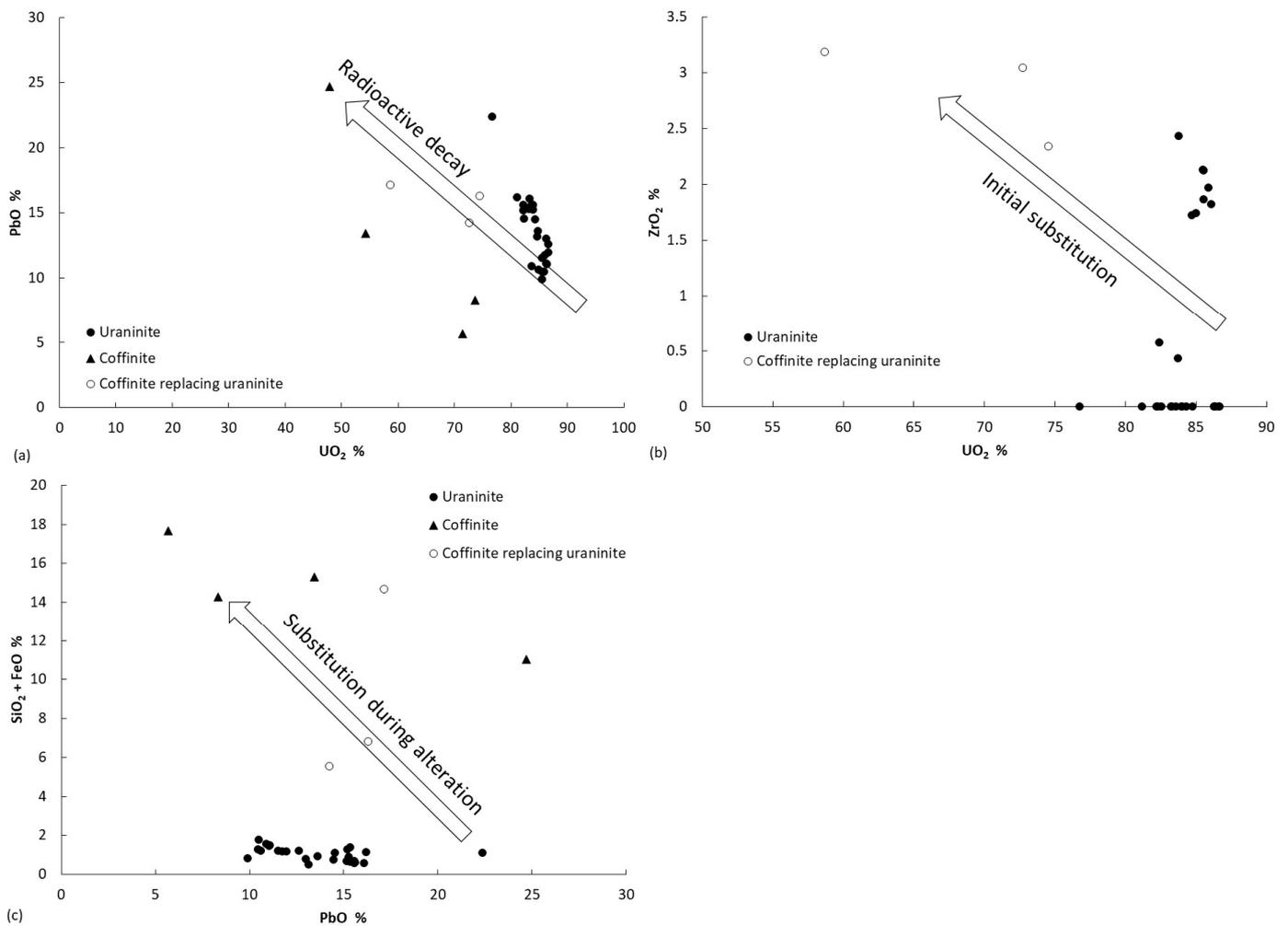
Figure 9. (**a**) Inverse relationship in the PbO-UO$_2$ diagram suggesting Pb in uraninite is related to radioactive decay. (**b**) Initial substitution of U by Zr. (**c**) Inverse relationship between PbO and SiO$_2$ + FeO represented mainly by coffinite-bearing samples.

Skutterudite has low Ni (<0.35%) but high S (4.30%–8.42%), which yields a mean formula of Co$_{1.06}$Fe$_{0.26}$Ni$_{0.01}$S$_{0.56}$As$_{2.11}$. The Port Radium cobaltite has 0.90%–6.44% Fe and up to 8.94% Ni with a mean formula of Co$_{1.04}$Fe$_{0.08}$Ni$_{0.20}$As$_{1.45}$S$_{1.23}$ (Table 9); traces of Cu and Sb are also found in cobaltite.

The composition of the unique minerals is different than the known minerals of the Fe-Co-Ni-As-S system at Port Radium: mineral X1 with a mean formula of Co$_{0.67}$Ni$_{0.32}$Fe$_{0.02}$S$_{0.19}$As$_{2.80}$, mineral X2 with a mean formula of Ni$_{0.85}$Co$_{0.15}$S$_{0.39}$As$_{1.60}$, and mineral X3 has a mean formula of Ni$_{0.69}$Co$_{0.31}$S$_{0.47}$As$_{1.52}$ (Table 10). These three minerals plot on separate fields in the Co-As-S, Ni-As-S, and As-Ni-Co diagrams (Figure 10). In the As/S vs. Ni/Co plot, these unnamed sulfarsenides plot on discrete fields in the central part of the graph (Figure 11).

Table 7. Representative analyses (in weight%) of the Port Radium siegenite, niccolite, rammelsbergite, and gersdorffite.

|	Siegenite (Ni,Co)$_3$S$_4$				Nickeline NiAs				Rammelsbergite NiAs$_2$				Gersdorffite NiAsS				Cobaltoan Gersdorffite (NiCo)AsS
Sample	126-PR-1-5	126-PR-1-6	126-PR-2-1	126-PR-2-5	183B-PR-2-1	183B-PR-2-2	183B-PR-2-4	183B-PR-2-15	183B-PR-2-6	183C-PR-1-29	183B-PR-2-17	183B-PR-2-7	183B-PR-2-10	183B-PR-2-11	183B-PR-2-13	183B-PR-2-18	126-PR-3-3
As	<0.25	<0.25	<0.25	<0.25	55.65	55.36	55.26	55.61	71.35	69.83	69.83	70.1	47.56	47.6	49.45	46.92	42.88
S	39.58	39.05	38.98	42.68	0.65	<0.20	<0.20	<0.20	0.69	1.31	0.89	0.91	17.49	17.5	16.57	18.28	19.74
Fe	2.19	2.23	1.67	1.56	<0.20	<0.20	<0.20	<0.20	<0.20	<0.20	<0.20	<0.20	<0.20	<0.20	<0.20	<0.20	2.58
Co	31.72	31.45	32.05	31.36	0.82	0.22	<0.20	<0.20	1.51	0.25	0.78	2.43	0.20	0.20	0.44	0.30	12.38
Ni	25.41	25.28	26.2	25.61	41.46	43.61	43.35	43.06	26.64	27.85	27.79	25.53	33.88	33.86	32.98	34.24	21.38
Cu	0.37	0.30	<0.20	<0.20	<0.20	<0.20	<0.20	<0.20	<0.20	<0.20	<0.20	<0.20	<0.20	<0.20	<0.20	<0.20	1.90
Total	99.28	98.31	98.89	101.21	98.58	99.19	98.61	98.67	100.19	99.24	99.29	98.97	99.13	99.16	99.44	99.74	100.86
	Number of ions based on 7 atoms				Number of ions based on 2 atoms				Number of ions based on 3 atoms				Number of ions based on 3 atoms				
As	0.000	0.000	0.000	0.000	1.001	0.995	0.999	1.006	1.966	1.926	1.933	1.949	1.081	1.082	1.134	1.053	0.934
S	3.839	3.828	3.806	4.003	0.027	0.000	0.000	0.000	0.044	0.084	0.058	0.059	0.929	0.930	0.888	0.958	1.005
Fe	0.122	0.126	0.094	0.084	0.000	0.000	0.000	0.000	0.000	0.000	0.000	0.000	0.000	0.000	0.000	0.000	0.075
Co	1.674	1.678	1.703	1.600	0.019	0.005	0.000	0.000	0.053	0.009	0.027	0.086	0.006	0.006	0.013	0.009	0.343
Ni	1.347	1.354	1.398	1.312	0.952	1.000	1.001	0.994	0.937	0.981	0.982	0.906	0.983	0.983	0.965	0.981	0.595
Cu	0.018	0.015	0.000	0.000	0.000	0.000	0.000	0.000	0.000	0.000	0.000	0.000	0.000	0.000	0.000	0.000	0.048

Table 8. Composition (in weight%) of the Port Radium clinosafflorite and safflorite.

	Clinosafflorite CoAs$_2$				Safflorite (Co,Ni,Fe)As$_2$			
Sample	183B-PR-1-21	183B-PR-1-22	183B-PR-1-24	183B-PR-1-25	183C-PR-4-20	183C-PR-4-21	183C-PR-4-22	183C-PR-4-23
As	71.83	70.55	67.84	69.72	69.78	67.61	69.24	67.61
S	0.81	0.33	1.93	0.56	1.00	1.27	0.56	1.89
Fe	2.19	1.44	2.32	3.10	3.23	3.25	2.25	2.44
Co	25.57	25.53	26.28	24.21	22.13	20.59	20.61	20.52
Ni	<0.20	0.25	0.26	1.20	3.52	4.50	6.14	5.75
Cu	0.36	0.30	<0.20	0.48	<0.20	<0.20	<0.20	<0.20
Sb	<0.25	0.52	<0.25	<0.25	<0.25	<0.25	<0.25	<0.25
Au	<0.30	<0.30	<0.30	<0.30	<0.30	1.19	<0.30	<0.30
Total	100.76	98.94	98.62	99.26	99.69	98.40	98.80	98.21

Table 8. *Cont.*

	Clinosafflorite CoAs$_2$					Safflorite (Co,Ni,Fe)As$_2$		
	Number of ions based on 3 atoms					Number of ions based on 3 atoms		
As	1.966	1.984	1.864	1.936	1.919	1.890	1.930	1.865
S	0.052	0.022	0.124	0.036	0.064	0.083	0.036	0.122
Fe	0.080	0.054	0.085	0.115	0.120	0.122	0.084	0.090
Co	0.890	0.913	0.918	0.854	0.774	0.732	0.731	0.720
Ni	0.000	0.009	0.009	0.043	0.124	0.161	0.219	0.203
Cu	0.012	0.010	0.000	0.016	0.000	0.000	0.000	0.000
Sb	0.000	0.009	0.000	0.000	0.000	0.000	0.000	0.000
Au	0.000	0.000	0.000	0.000	0.000	0.013	0.000	0.000

Table 9. Representative analyses (in weight%) of the Port Radium skutterudite and cobaltite.

|	Skuterrudite (Co,Ni,Fe)As$_{3-X}$					Cobaltite (Co,Ni,Fe)AsS			
Sample	183C-PR-1-13	183C-PR-1-14	183C-PR-4-17	183C-PR-4-18	183C-PR-4-19	183C-PR-4-14	183C-PR-1-4	183C-PR-1-9	183C-PR-1-12
As	60.55	60.75	62.81	67.40	61.94	47.43	48.63	48.50	46.41
S	8.42	8.31	6.96	4.30	7.77	18.57	17.07	17.22	18.33
Fe	5.00	5.77	5.74	6.74	5.75	6.44	1.22	1.37	0.90
Co	26.39	26.37	24.59	21.88	24.68	27.76	26.72	27.13	25.09
Ni	0.28	<0.20	0.34	0.35	0.25	<0.20	6.17	5.85	8.94
Cu	<0.20	<0.20	<0.20	<0.20	<0.20	0.36	<0.20	<0.20	<0.20
Sb	0.29	<0.25	<0.25	<0.25	<0.25	<0.25	<0.25	<0.25	0.38
Total	100.92	101.19	100.44	100.67	100.39	100.55	99.82	100.06	99.66
	Number of ions based on 4 atoms					Number of ions based on 4 atoms			
As	2.002	2.001	2.121	2.349	2.073	1.404	1.474	1.464	1.386
S	0.650	0.640	0.549	0.351	0.608	1.284	1.209	1.214	1.279
Fe	0.222	0.255	0.260	0.315	0.258	0.256	0.050	0.055	0.036
Co	1.109	1.104	1.056	0.969	1.050	1.045	1.029	1.041	0.952
Ni	0.012	0.000	0.015	0.016	0.011	0.000	0.239	0.225	0.341
Cu	0.000	0.000	0.000	0.000	0.000	0.012	0.000	0.000	0.000
Sb	0.006	0.000	0.000	0.000	0.000	0.000	0.000	0.000	0.007

Table 10. Three unique minerals of the Fe-Co-Ni-As-S system from the Port Radium deposit (in weight%).

Mineral X1 $Co_{0.67}Ni_{0.32}Fe_{0.02}S_{0.19}As_{2.80}$										
Sample	183C-PR-3-1	183C-PR-3-2	183C-PR-3-3	183C-PR-4-1	183C-PR-4-2	183C-PR-4-3	183C-PR-4-4	183C-PR-3-4	183C-PR-3-5	183C-PR-3-6
As	76.14	73.69	74.36	74.52	75.06	75.52	77.08	77.31	77.05	77.33
S	2.09	2.98	3.04	3.13	2.80	2.79	1.32	1.24	1.18	1.57
Fe	0.34	0.42	0.58	0.46	0.59	0.46	0.41	0.50	0.32	0.48
Co	14.47	15.67	16.62	17.50	15.98	15.00	11.94	11.92	11.74	12.38
Ni	6.53	5.92	5.24	4.30	4.61	5.63	8.59	8.70	8.75	8.43
Sb	<0.25	0.35	<0.25	<0.25	<0.25	<0.25	<0.25	<0.25	<0.25	<0.25
Totals	99.57	99.04	99.84	99.90	99.04	99.40	99.34	99.68	99.04	100.19
Number of ions based on 4 atoms										
As	2.814	2.706	2.703	2.705	2.765	2.774	2.885	2.886	2.898	2.860
S	0.181	0.256	0.258	0.265	0.241	0.239	0.116	0.109	0.104	0.136
Fe	0.017	0.021	0.028	0.023	0.029	0.023	0.020	0.025	0.016	0.024
Co	0.680	0.732	0.768	0.808	0.748	0.700	0.568	0.566	0.562	0.582
Ni	0.308	0.278	0.243	0.199	0.217	0.264	0.410	0.415	0.420	0.398
Sb	0.000	0.008	0.000	0.000	0.000	0.000	0.000	0.000	0.000	0.000
As + S	2.995	2.962	2.961	2.971	3.006	3.013	3.001	2.995	3.002	2.996
Fe + Co + Ni + Sb	1.005	1.038	1.039	1.029	0.994	0.987	0.999	1.005	0.998	1.004

Mineral X2 $Ni_{0.85}Co_{0.15}S_{0.39}As_{1.60}$						Mineral X3 $Ni_{0.69}Co_{0.31}S_{0.47}As_{1.52}$			
Sample	183C-PR-1-32	183C-PR-1-1	183C-PR-1-20	183C-PR-1-31	183C-PR-1-6	183C-PR-1-30	183C-PR-1-2	183C-PR-1-2A	183C-PR-1-2B
As	61.47	62.25	62.51	61.69	63.51	59.10	61.16	61.23	59.57
S	7.04	7.11	6.56	6.49	5.10	8.46	7.76	7.65	8.24
Fe	bdl	bdl	bdl	bdl	bdl	bdl	bdl	bdl	bdl
Co	4.19	4.55	4.36	5.04	5.17	10.49	9.41	9.30	10.15
Ni	26.60	26.61	26.20	25.70	24.78	21.31	21.89	21.79	21.45
Sb	<0.25	<0.25	<0.25	<0.25	<0.25	0.33	<0.25	<0.25	<0.25
Totals	99.30	100.52	99.63	98.92	98.56	99.68	100.22	99.97	99.41
Number of ions based on 3 atoms						Number of ions based on 3 atoms			
As	1.573	1.574	1.605	1.595	1.677	1.482	1.539	1.547	1.500
S	0.421	0.420	0.394	0.392	0.315	0.496	0.456	0.452	0.485
Fe	0.000	0.000	0.000	0.000	0.000	0.000	0.000	0.000	0.000
Co	0.136	0.146	0.142	0.166	0.174	0.335	0.301	0.299	0.325
Ni	0.869	0.859	0.859	0.848	0.835	0.682	0.703	0.703	0.690
Sb	0.000	0.000	0.000	0.000	0.000	0.005	0.000	0.000	0.000
As + S	1.995	1.995	1.999	1.986	1.991	1.978	1.996	1.999	1.985
Fe + Co + Ni + Sb	1.005	1.005	1.001	1.014	1.009	1.022	1.004	1.001	1.015
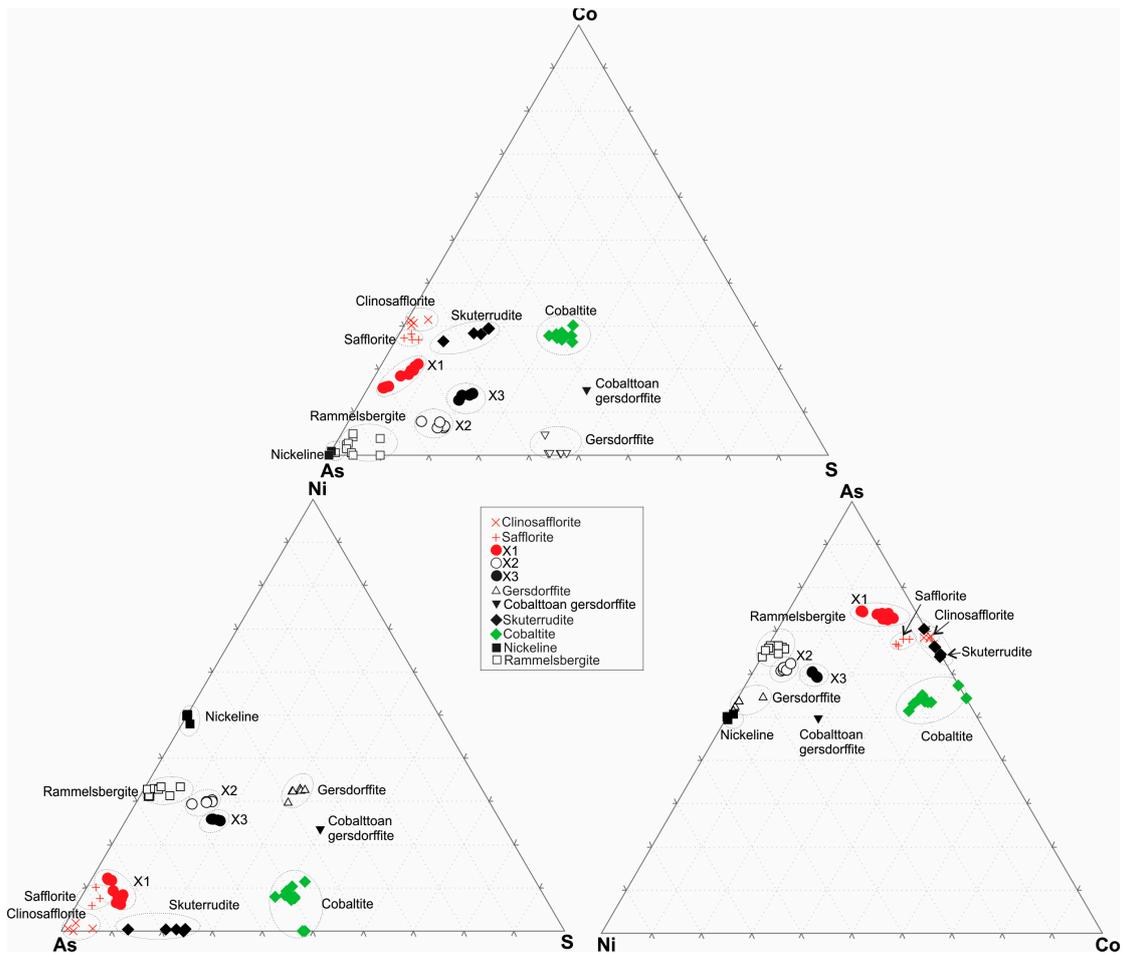
Figure 10. The Port Radium sulfarsenides in the Co-As-S, Ni-As-S, and As-Ni-Co diagrams showing discrete composition of three unique minerals. Data plotted based on atoms per formula unit (apfu).
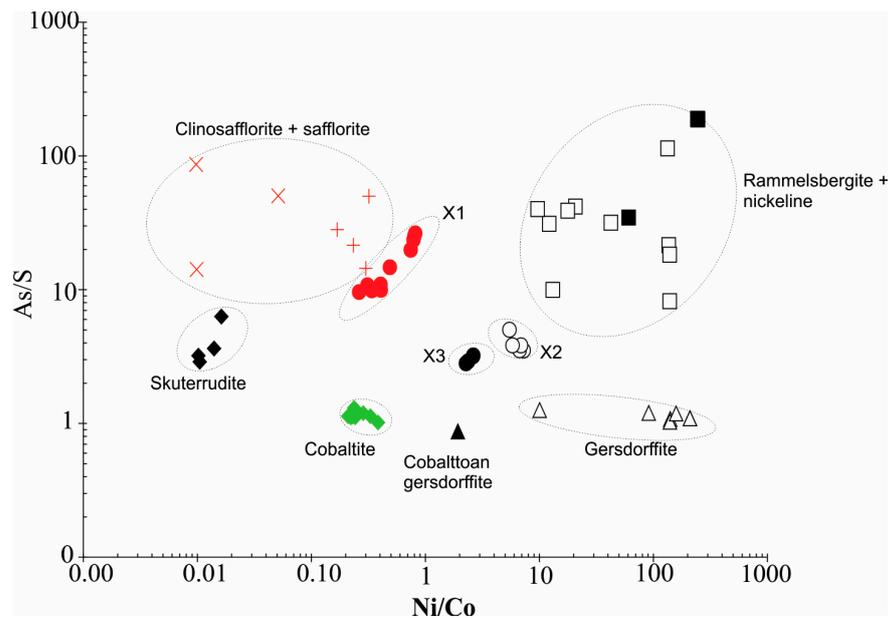
Figure 11. As/S vs. Ni/Co plot showing composition of the Port Radium sulfarsenides. The unique minerals plot in the central part of the graph. Ratios are calculated using apfu. Symbols are the same as those in Figure 10.

5. Discussion

The Great Bear magmatic zone experienced prolonged arc-related magmatism that intruded felsic-intermediate plutonic bodies into the ~1.87 Ga Echo Bay and Port Radium supracrustal sub-aerial sedimentary rocks and volcanic suites. This magmatism created a perfect geological environment for the formation of a variety of ore deposits and introduced a substantial number of metals such as Fe, Cu, Pb, Zn, Ni, Co, U, Bi, and Ag [20,22,33]. The Richardson high heat production pluton located 9 km south of Port Radium (Figure 1) belongs to the 1.85 Ga suite of plutons and is enriched in some of these metals (particularly U and Th) and may have partially been the source of some of these metals [50]. Such plutons forming the later-stage batholiths of the GBMZ may have induced renewed fluid circulation and mineralization. Renewed fluid circulation at the time of emplacement may have led to the ingress of some of these metals in the hydrothermal system or may have induced a new stage of fluid circulation that remobilized the primary endowment of the MIAC system into vein mineralization [33] or the veins may be formed much later as were some of the Eldorado veins [27,51]. Based on the presence of hydrocarbon in fluid inclusions, Trottier (2019) [51] interpreted that the metals were sourced within the overlying late Paleoproterozoic Hornby Bay Basin.

The classification of ore deposits within MIAC systems includes the IOCG deposits and a wide variety of other metasomatic deposit types [33,52]. Williams et al. (2005) [53] define IOCG deposits as having Cu ± Au as economic metals in structurally controlled hydrothermal veins, breccias, and/or replacement ore bodies with abundant magnetite and/or hematite (>15%) that have low Ti content. These deposits have no clear spatial associations with igneous intrusions (in contrast to porphyry and some skarn ore deposits) [53]. Skirrow (2022) [54] proposed a new classification for components of the MIAC systems, which he referred to as a Cu-Au-Fe mineral system that is subclassified based on geological/tectonic settings and predominant metals and minerals. These subclasses include (1) IOCG deposits as a major part of this mineral system and (2) Fe-sulfide Cu-Au deposits lacking significant iron oxides. This classification discriminates these deposits from porphyry Cu (-Au), skarn Fe-Cu (-Au), and iron oxide-apatite deposits, although there are some shared features.

Hydrothermal mineralogy and alteration facies of the Port Radium–Echo Bay district are similar to other GBMZ systems and to global IOCG deposits and host systems. The main ore mineralization occurred during epithermal veining, which occurred after a pervasive and intensive IOCG-style MIAC hydrothermal alteration, including albitic, magnetite-actinolite-apatite, potassic, phyllic, and propylitic. Various types of veins and hydrothermal assemblages formed during fluid–rock interactions and the evolution of the Port Radium hydrothermal system. These complex textural and compositional variations in the ore mineralogy reflect changes in temperature and chemical activities in the system [22,25,38].

Although sulfide mineralization is younger than magnetite-actinolite-apatite alteration, drill core logging and drill assay data of IOCG-style deposits in GBMZ [38,55,56], indicate that magnetite-actinolite-apatite zones always have high base metal concentrations. This may suggest that either both magnetite-actinolite-apatite and sulfide mineralizations utilized the same channels for precipitation or magnetite-actinolite-apatite prepared the ground for sulfide mineralization by alteration of the country rocks, which were subsequently fractured easily, forming channels for movement of the base metal-bearing hydrothermal solution. As the hydrothermal system evolved, the magnetite content of the magnetite-actinolite-apatite alteration decreased, and sulfide mineralization progressed. This manifests as magnetite-actinolite-apatite transitioning into actinolite-apatite-pyrrhotite-pyrite-chalcopyrite, possibly reflecting the change in the fugacity of oxygen and sulfur in the hydrothermal system.

Sulfide and sulfarsenide mineralization in the strongly altered wall rocks occurred, possibly due to the reaction of the hydrothermal solution with the country rocks. Such reactions commonly formed fine-grained hydrothermal assemblages at Port Radium (Figure 6d). In contrast, similar minerals precipitate as coarser grains in the veins due to boiling or

sudden changes in the pressure and temperature of the hydrothermal fluid [38]. Intense brecciation of the immediate wall rocks of the veins (Figure 6a) suggests high fluid pressure during hydrothermal activity that caused the hydrofracturing of the surrounding rocks. Propylitic alteration of the wall rock fragments shows that the main ore mineralization of Port Radium occurred after propylitic alteration. The cross-cutting relationship and textural features show that uranium mineralization occurred after sulfides and sulfarsenide mineralization in the same veins at shallow depths. This temporal and spatial relationship between uranium and sulfides-sulfarsenide mineralization at Port Radium can be used as an exploration tool for uranium mineralization in the region or worldwide. In addition, these hydrothermal systems can be identified based on their magnetic anomaly caused by the high amount of magnetite in the magnetite-actinolite-apatite zones (Figure 3).

The Port Radium hydrothermal system was enriched in Ni and Co; as a result, not only the common sulfides, such as pyrite and pyrrhotite, but also sphalerite, chalcopyrite, arsenopyrite, tetrahedrite, emplectite, and aikinite have traces of these metals (as substitutes for Fe and possibly Zn and Cu). However, most of these minerals have nearly stoichiometric compositions.

Safflorite, clinosafflorite, gersdorffite, skutterudite, cobaltite, nickeline, and rammelsbergite are common minerals of the Fe-Co-Ni-As-S system that are found at Port Radium. Composition of these minerals changes rapidly even in a micrometer scale, ranging from almost pure end members to mixed solid solutions; gersdorffite ($Ni_{0.96}Co_{0.02}As_{1.10}S_{0.91}$) and cobaltoan gersdorffite ($Ni_{0.60}Co_{0.34}Fe_{0.08}As_{0.93}S_{1.01}$) are examples of such change at Port Radium. Similarly, Kiefer et al. (2017) [5] reported Co-rich gersdorffite ($Ni_{0.32}Co_{0.49}Fe_{0.23}As_{1.00}S_{0.95}$) from Dobšiná, Slovakia. This variability in composition is a common feature of the minerals in the Fe-Co-Ni-As-S system [5,12].

At Port Radium, krutovite (isotropic diarsenide $NiAs_2$) was not found, whereas rammelsbergite (strongly anisotropic diarsenide $NiAs_2$) is a common mineral. The Port Radium rammelsbergite is generally Fe-Co poor with Fe + Co range of 0.00 to 0.11 apfu (average 0.04 apfu). The Dobšiná rammelsbergite has >0.1 Fe + Co apfu [5]. It appears that the composition of rammelsbergite varies significantly from deposit to deposit, which may suggest not only solid solution but also the physico-chemical conditions of each deposit affect the composition of this mineral. The Port Radium skutterudite is Ni-poor ($Co_{1.06}Fe_{0.26}Ni_{0.01}S_{0.56}As_{2.11}$) and its Fe content is not high enough to be a ferroskutterudite. Compared to skutterudite, cobaltite has higher Ni with up to 0.34 apfu.

Three unique minerals show distinct compositional differences with known minerals of this system (Figures 10 and 11). These minerals have not been reported in experimental and field-based papers, e.g., [5,8,9,11,12]. In mineral X1 ($Co_{0.67}Ni_{0.32}Fe_{0.02}S_{0.19}As_{2.80}$), the sum of Co + Ni + Fe and As + S are 1.01 and 2.99, respectively. This composition is consistent with stoichiometric skutterudite [$(Co,Ni,Fe)As_{3-x}$]; however, this mineral has higher sulfur content than skutterudite. A similar S-Co-rich mineral (as skutterudite) with a composition of $Co_{0.65}Ni_{0.21}Fe_{0.22}S_{0.15}As_{2.77}$ was reported by Kiefer et al. (2017) [5].

Minerals X2 ($Ni_{0.85}Co_{0.15}S_{0.39}As_{1.60}$) and X3 ($Ni_{0.69}Co_{0.31}S_{0.47}As_{1.52}$) are chemically comparable to the Port Radium rammelsbergite ($Ni_{0.95}Co_{0.04}S_{0.08}As_{1.92}$) with substantial addition of S and Co. Addition of S to rammelsbergite by hydrothermal solution and formation of gersdorffite has already been documented at Port Radium (Figure 6f). Kiefer et al. (2017) [5] calculated the mean composition of 81 rammelsbergite from Dobšiná, Slovakia, as $Ni_{0.97}Fe_{0.02}Co_{0.03}As_{1.90}S_{0.07}$. They reported that the maximum concentration of Co and Fe in rammelsbergite was low, at 0.07 and 0.05 apfu, respectively. In terms of composition, mineral X2 and X3 could be solid solution products of gersdorffite-cobaltite or safflorite-rammelsbergite. The addition or vast substitution of As-S and Ni-Co-Fe in the Fe-Co-Ni-As-S system changes unit cells, and forms different minerals [12]. These changes may affect optical properties, including anisotropism of the sulfarsenide [5].

6. Conclusions

The Echo Bay and Port Radium volcano-sedimentary sequence and their sub-volcanic intrusions coevally formed a regional metasomatic mineral system that has developed a wide range of mineralization styles, including IOCG (K2 and Mag Hill showings) and polymetallic skarn as well as the Port Radium epithermal five-element veins. This metasomatic mineral system precipitated a variety of hydrothermal alteration facies from albitic to magnetite-actinolite-apatite, potassic ± albitic, phyllic, and propylitic. Scarce to minor sulfide minerals formed during these alteration events characterize the primary MIAC system. The main ore mineralization occurred during the epithermal stage of the MIAC system when various arsenide/sulfarsenide minerals formed with or without uraninite. Some of these veins may result from elements remobilization during the prolonged magmatic, hydrothermal, and structural activities in the region. These veins are spatially associated with magnetic anomalies due to the high magnetite of magnetite-actinolite-apatite zone in the Port Radium area, which can be used as an exploration tool.

In addition to common arsenide and sulfarsenide minerals, three unique minerals are found. Mineral X1 ($Co_{0.67}Ni_{0.32}Fe_{0.02}S_{0.19}As_{2.80}$) could be a sulfur-rich skutterudite. Minerals X2 ($Ni_{0.85}Co_{0.15}S_{0.39}As_{1.60}$) and X3 ($Ni_{0.69}Co_{0.31}S_{0.47}As_{1.52}$) could be a solid solution of gersdorffite-cobaltite or safflorite-rammelsbergite. These indicate that a wide range of minerals, some of which are yet to be determined, can form in the Fe-Co-Ni-As-S system.

Author Contributions: A.K.S. carried out fieldwork, analysis and the interpretation of data. L.Z. helped in the mineral analysis and partial mineral calculation and interpretation. G.Z. and X.M. helped with the methodology. All authors have read and agreed to the published version of the manuscript.

References

1. Wagner, T.; Lorenz, J. Mineralogy of complex Co–Ni–Bi vein mineralization, Bieber deposit, Spessart, Germany. *Mineral. Mag.* **2002**, *66*, 385–407. [CrossRef]
2. Melekestseva, I.Y.; Zaikov, V.V.; Tesalina, S.G. Sulfoarsenides and arsenides of Co, Fe and Ni in ores of Ishkininsk cobalt-copper massive sulfide deposit of southern Urals. *Zap. Vserossiiskogo Mineral. Obs.* **2003**, *132*, 66–77.
3. Parviainen, A.; Gervilla, F.; Melgarejo, J.C.; Johanson, B. Low-temperature, platinum-group elements-bearing Ni arsenide assemblage from the Atrevida mine (Catalonian Coastal Ranges, NE Spain). *Neues Jahrb. Für Mineral. Abh.* **2008**, *185*, 33–49. [CrossRef]
4. Gervilla, F.; Fanlo, I.; Colás, V.; Subías, I. Mineral compositions and phase relations of Ni-Co-Fe arsenide ores from the Aghbar Mine, Bou Azzer, Marocco. *Can. Mineral.* **2012**, *50*, 447–470. [CrossRef]
5. Kiefer, S.; Majzlan, J.; Chovan, M.; Stevko, M. Mineral compositions and phase relations of the complex sulfarsenides and arsenides from Dobsina (Western Carpathians, Slovakia). *Ore Geol. Rev.* **2017**, *89*, 894–908. [CrossRef]
6. Rezazadeh, S.; Hosseinzadeh, M.R.; Raith, J.G.; Moayyed, M. Mineral chemistry and phase relations of Co–Ni arsenides and sulfarsenides from the Baycheh-Bagh deposit, Zanjan province, Iran. *Ore Geol. Rev.* **2020**, *127*, 103836. [CrossRef]

7.　Tourneur, E.; Chauvet, A.; Kouzmanov, K.; Tuduri, J.; Paquez, C.; Sizaret, S.; Karfal, A.; Moundi, Y.; El Hassani, A. Co-Ni-arsenide mineralisation in the Bou Azzer district (Anti-Atlas, Morocco): Genetic model and tectonic implications. *Ore Geol. Rev.* **2021**, *134*, 104128. [CrossRef]

8.　Fuess, H.; Kratz, T.; Toepel-Schadt, J.; Miehe, G. Crystal structure refinement and electron microscopy of arsenopyrite. *Z. Für Krist.* **1987**, *179*, 335–346. [CrossRef]

9.　Fleet, M.E.; Burns, P.C. Structure and twinning of cobaltite. *Can. Mineral.* **1990**, *28*, 719–723.

10.　Posfai, M.; Sharp, T.G.; Kontny, A. Pyrrhotite varieties from the 9.1 km deep borehole of the KTB project. *Am. Mineral.* **2002**, *85*, 1406–1415. [CrossRef]

11.　Hem, S.R.; Makovicky, E. The system Fe–Co–Ni–As–S. II. Phase relations in the $(FeCo, Ni)As_{1.5}S_{0.5}$ section at 650° and 500 °C. *Can. Mineral.* **2004**, *42*, 63–86. [CrossRef]

12.　Hem, S.R. Solid solutions in the Fe–Co–Ni–As–S system. *Chem. Geol.* **2006**, *225*, 291–303. [CrossRef]

13.　Somarin, A.K.; Zhou, L. Hydrothermal Mineralization and Mineral Chemistry of Arsenides and Sulfarsenides in the Fe-Co-Ni-As-S System and Introduction of Three Unknown Minerals from the Port Radium IOCG Deposit, Northwest Territories, Canada. Research Square Preprint. 2022. Available online: https://www.researchsquare.com/article/rs-1551126/v1 (accessed on 1 November 2023).

14.　Hildebrand, R.S.; Hoffman, P.F.; Bowring, S.A. The Calderian orogeny in Wopmay orogen (1.9 Ga), northwestern Canadian Shield. *Geol. Soc. Am. Bull.* **2010**, *122*, 794–814. [CrossRef]

15.　Hildebrand, R.S.; Hoffman, P.F.; Bowring, S.A. Tectonomagmatic evolution of the 1.9 Ga Great Bear magmatic zone, Wopmay orogen, northwestern Canada. *J. Volcan. Geoth. Res.* **1987**, *32*, 99–118. [CrossRef]

16.　Gandhi, S.S.; Mortensen, J.K.; Prasad, N.; van Breemen, O. Magmatic evolution of the southern Great Bear continental arc, northwestern Canadian Shield: Geochronological constraints. *Can. J. Earth Sci.* **2001**, *38*, 767–785. [CrossRef]

17.　Ootes, L.; Davis, W.J.; Jackson, V.A.; van Breemen, O. Chronostratigraphy of the Hottah terrane and Great Bear magmatic zone of Wopmay Orogen, Canada, and exploration of a terrane translation model. *Can. J. Earth Sci.* **2015**, *52*, 1062–1092. [CrossRef]

18.　Ootes, L.; Snyder, D.; Davis, W.J.; Acosta-Góngora, P.; Corriveau, L.; Mumin, A.H.; Montreuil, J.F.; Gleeson, S.A.; Samson, I.A.; Jackson, V.A. A Paleoproterozoic Andean-type iron oxide copper-gold environment, the Great Bear magmatic zone, Northwest Canada. *Ore Geol. Rev.* **2017**, *81*, 123–139. [CrossRef]

19.　Montreuil, J.F.; Corriveau, L.; Davis, W.J. Tectonomagmatic Evolution of the Southern Great Bear Magmatic Zone (Northwest Territories, Canada): Implications for the Genesis of Iron Oxide-Alkali–Altered Hydrothermal Systems. *Econ. Geol.* **2016**, *111*, 2111–2138. [CrossRef]

20.　Mumin, A.H.; Somarin, A.K.; Jones, B.; Corriveau, L.; Ootes, L.; Camier, J. The IOCG-porphyry-epithermal continuum in the Great Bear Magmatic Zone, Northwest Territories, Canada. In *Exploring for Iron Oxide Copper-Gold Deposits: Canada and Global Analogue*; Corriveau, L., Mumin, A.H., Eds.; Short Course Notes; Geological Association of Canada: Toronto, ON, Canada, 2010; Volume 20, pp. 59–78.

21.　Montreuil, J.F.; Corriveau, L.; Potter, E.G. Formation of albitite-hosted uranium within IOCG systems: The Southern Breccia, Great Bear magmatic zone, Northwest Territories, Canada. *Miner. Depos.* **2015**, *50*, 293–325. [CrossRef]

22.　Corriveau, L.; Montreuil, J.F.; Potter, E.G. Alteration facies linkages among IOCG, IOA and affiliated deposits in the Great Bear magmatic zone, Canada. In *Proterozoic Iron Oxide-Apatite (±REE) and Iron Oxide-Copper-Gold and Affiliated Deposits of Southeast Missouri, USA, and the Great Bear Magmatic Zone, Northwest Territories, Canada*; Slack, J., Corriveau, L., Hitzman, M., Eds.; Economic Geology: Littleton, CO, USA, 2016; Volume 111, pp. 2045–2072.

23.　Corriveau, L.; Montreuil, J.F.; Potter, E.G.; Blein, O.; De Toni, A.F. Mineral systems with IOCG and affiliated deposits: Part 3—*Metal* pathways and ore deposit model. In *Mineral Systems with Iron Oxide Copper-Gold (IOCG) and Affiliated Deposits*; Corriveau, L., Potter, E.G., Mumin, A.H., Eds.; Special Paper; Geological Association of Canada: Toronto, ON, Canada, 2022; Volume 52, pp. 205–245.

24.　Mumin, A.H.; Corriveau, L.; Somarin, A.K.; Ootes, L. IOCG-type polymetallic mineralization in the Contact Lake Belt, Great Bear Magmatic Zone, Northwest Territories. *Expl. Min. Geol.* **2007**, *16*, 187–208. [CrossRef]

25.　Corriveau, L.; Williams, P.J.; Mumin, A.H. Alteration vectors to IOCG mineralization: From uncharted terranes to deposits. In *Exploring for Iron Oxide Copper-Gold Deposits: Canada and Global Analogues*; Corriveau, L., Mumin, A.H., Eds.; Short Course Notes; Geological Association of Canada: Toronto, ON, Canada, 2010; Volume 20, pp. 89–110.

26.　Corriveau, L.; Montreuil, J.F.; De Toni, A.F.; Potter, E.G.; Percival, J.B. Mapping mineral systems with IOCG and affiliated deposits: A facies approach. In *Mineral Systems with Iron Oxide Copper-Gold (IOCG) and Affiliated Deposits*; Corriveau, L., Potter, E.G., Mumin, A.H., Eds.; Special Paper; Geological Association of Canada: Toronto, ON, Canada, 2022; Volume 52, pp. 69–111.

27.　Gandhi, S.S.; Potter, E.G.; Fayek, M. New constraints on genesis of the polymetallic veins at Port Radium, Great Bear Lake, Northwest Canadian Shield. *Ore Geol. Rev.* **2018**, *96*, 28–47. [CrossRef]

28.　Badham, J.P.N. Mineralogy, paragenesis and origin of the Ag–Ni, Co arsenide mineralization, Camsell River, N.W.T., Canada. *Miner. Depos.* **1975**, *10*, 153–175. [CrossRef]

29.　Hoffman, P.F. Wopmay orogen: A Wilson cycle of early Proterozoic age in the northwest of the Canadian Shield. In *The Continental Crust and Its Mineral Deposits*; Strangway, D.W., Ed.; Special Paper; Geological Association of Canada: Toronto, ON, Canada, 1980; Volume 20, pp. 523–549.

30. Hildebrand, R.S. Early Proterozoic LaBine Group of Wopmay orogen: Remnant of a continental volcanic arc developed during oblique convergence. In *Proterozoic Basins in Canada*; Campbell, F.H.A., Ed.; Geological Survey of Canada Paper; Geological Survey of Canada: Ottawa, ON, Canada, 1981; Volume 81, pp. 133–156.

31. Hildebrand, R.S. Geology of the Echo Bay-MacAlpine Channel Area, District of Mackenzie. Geological Survey of Canada, Map 1546A, 1983, Scale 1:50,000. Available online: https://www.researchgate.net/profile/Robert-Hildebrand-2/publication/2696 33529_Geology_Calder_River_map_area/links/549087a60cf214269f26b017/Geology-Calder-River-map-area.pdf (accessed on 1 November 2023).

32. Hildebrand, R.S. Kiruna-type deposits: Their origin and relationship to intermediate subvolcanic plutons in the Great Bear Magmatic Zone, northwest Canada. *Econ. Geol.* **1986**, *81*, 640–659. [CrossRef]

33. Corriveau, L.; Montreuil, J.F.; Blein, O.; Ehrig, K.; Potter, E.G.; Fabris, A.; Clark, J. Mineral systems with IOCG and affiliated deposits: Part 2—*Geochemical* footprints. In *Mineral Systems with Iron Oxide Copper-Gold (IOCG) and Affiliated Deposits*; Corriveau, L., Potter, E.G., Mumin, A.H., Eds.; Special Paper; Geological Association of Canada: Toronto, ON, Canada, 2022; Volume 52, pp. 159–204.

34. Corriveau, L.; Montreuil, J.F.; Potter, E.G.; Ehrig, K.; Clark, J.; Mumin, A.H.; Williams, P.J. Mineral systems with IOCG and affiliated deposits: Part 1–metasomatic footprints of alteration facies. In *Mineral Systems with Iron Oxide Copper-Gold (IOCG) and Affiliated Deposits*; Corriveau, L., Potter, E.G., Mumin, A.H., Eds.; Special Paper; Geological Association of Canada: Toronto, ON, Canada, 2022; Volume 52, pp. 113–158.

35. Montreuil, J.F.; Corriveau, L.; Potter, E.G.; De Toni, A.F. On the relation between alteration facies and metal endowment of iron oxide–alkali-altered systems, southern Great Bear magmatic zone (Canada). In *Proterozoic Iron Oxide-Apatite (±REE) and Iron Oxide-Copper-Gold and Affiliated Deposits of Southeast Missouri, USA, and the Great Bear Magmatic Zone, Northwest Territories, Canada*; Slack, J., Corriveau, L., Hitzman, M., Eds.; Economic Geology: Littleton, CO, USA, 2016; Volume 111, pp. 2139–2168.

36. Potter, E.G.; Montreuil, J.F.; Corriveau, L.; Davis, W. The Southern Breccia metasomatic uranium system of the Great Bear magmatic zone, Canada: Iron oxide-copper-gold (IOCG) and albitite-hosted uranium linkages. *Geophys. Mono* **2019**, *242*, 109–130.

37. Potter, E.G.; Acosta-Góngora, P.; Corriveau, L.; Montreuil, J.F.; Yang, Z. Uranium enrichment processes in iron oxide and alkali-calcic alteration systems as revealed by uraninite trace element chemistry. In *Mineral Systems with Iron Oxide Copper-Gold (IOCG) and Affiliated Deposits*; Corriveau, L., Potter, E.G., Mumin, A.H., Eds.; Special Paper; Geological Association of Canada: Toronto, ON, Canada, 2022; Volume 52, pp. 325–345.

38. Somarin, A.K.; Mumin, A.H. P-T-composition and evolution of paleofluids in the Precambrian Mag Hill volcano-plutonic system, Northwest Territories, Canada. *Miner. Depos.* **2014**, *49*, 199–215. [CrossRef]

39. Kissin, S.A. Five-element (Ni-Co-As-Ag-Bi) Veins. *J. Geol. Assoc. Can.* **1992**, *19*, 113–124.

40. Cathro, R.J. Uranium production from East Germany, Czeckoslovakia, and Eldorado, Northwest Territories, after 1945. *Can. Inst. Min. Metal.* **2005**, *98*, 67–69.

41. Kidd, D.F.; Haycock, M.H. Mineragraphy of the ores of Great Bear Lake. *Bull. Geol. Soci. Am.* **1935**, *46*, 879–960. [CrossRef]

42. Hayward, N. 3D magnetic inversion of mineral prospects in the Great Bear magmatic zone, NT, Canada. *Geol. Surv. Can. Open File* **2013**, 7421. [CrossRef]

43. Hayward, N.; Tschirhart, V. A comparison of 3-D inversion strategies in the investigation of the 3-D density and magnetic susceptibility distribution in the Great Bear Magmatic Zone, Northwest Territories. *Geol. Surv. Can. Open File* **2023**, 8985. [CrossRef]

44. Mumin, A.H.; Phillips, A.; Katsuragi, C.J.; Mumin, A.; Ivanov, G. Geotectonic interpretation of the Echo Bay stratovolcano complex, northern Great Bear magmatic zone, NWT, Canada. *NWT Geosci. Off. Open File* **2014**, *2014–04*, 44.

45. Bailey, M. Ore Mineralogy and Uraninite Trace Element Chemistry of Hydrothermal Polymetallic U-Ag-(Co-Ni-As-Bi-Sb-Cu) Vein Deposits, Eldorado Mine, Port Radium, NWT. Unpublished Bachelor's Thesis, Saint Mary's University, Halifax, NS, Canada, 2017.

46. Somarin, A.K.; Mumin, A.H.; Zhou, L.; Chen, W.; Baig, A. Geochemistry of ore minerals and evolution of the Port Radium IOCG hydrothermal system, Great Bear Magmatic Zone, NWT, Canada. In Proceedings of the 2022 Goldschmidt Conference, Goldschmidt, HI, USA, 10–15 July 2022.

47. Whitney, D.A.; Bernard, W.; Evans, B.W. Abbreviations for names of rock-forming minerals. *Am. Mineral.* **2010**, *95*, 185–187. [CrossRef]

48. Hem, S.R.; Makovicky, E.; Gervilla, F. Compositional trends in Fe, Co and Ni sulfarsenides and their crystal-chemical implications: Results from the Arroyo de la Cueva deposits, Ronda peridotite, Southern Spain. *Can. Mineral.* **2001**, *39*, 831–853. [CrossRef]

49. Alexandre, P.; Kyser, K.; Layton-Matthews, D.; Brian, J. Chemical compositions of natural uraninite. *Can. Mineral.* **2016**, *53*, 595–622. [CrossRef]

50. Somarin, A.K.; Mumin, A.H. The Paleo-Proterozoic high heat production Richardson Granite, Great Bear Magmatic Zone, Northwest Territories, Canada: Source of U for Port Radium? *Res. Geol.* **2012**, *62*, 227–242. [CrossRef]

51. Trottier, C.R.M. Fluid Inclusion, Stable and Radiogenic Isotope, and Geochronological Investigation of the Polymetallic "Five-Element" Vein Deposit at the Eldorado Mine, Port Radium, Northwest Territories, Canada. Unpublished Master's Thesis, Saint Mary's University, Halifax, NS, Canada, 2019.

52. Hofstra, A.; Lisitsin, V.; Corriveau, L.; Paradis, S.; Peter, J.; Lauzière, K.; Lawley, C.; Gadd, M.; Pilote, J.; Honsberger, I.; et al. *Deposit Classification Scheme for the Critical Minerals Mapping Initiative Global Geochemical Database*; U.S. Geological Survey Open-File Report; U.S. Geological Survey: Reston, VA, USA, 2021; pp. 1–43. [CrossRef]

53. Williams, P.J.; Barton, M.D.; Fontboté, L.; de Haller, A.; Johnson, D.A.; Mark, G.; Marschik, R.; Oliver, N.H.S. Iron-oxide-copper-gold deposits: Geology, space-time distribution, and possible modes of origin. *Econ. Geol.* **2005**, *100*, 371–406.

54. Skirrow, R.G. Iron oxide copper-gold (IOCG) deposits—A review (part 1): Settings, mineralogy, ore geochemistry and classification. *Ore Geol. Rev.* **2022**, *140*, 104569. [CrossRef]

55. Somarin, A.K.; Mumin, A.H. Geochemistry and possible source of metals and alkalies for the Port Radium IOCG style hydrothermal system, Great Bear Magmatic Zone, Northwest Territories, Canada. In Proceedings of the Geological Association of Canada and Mineralogical Association of Canada Annual Meeting, Quebec City, QC, Canada, 19–23 May 2008.

56. Klapheke, M. Comparison of the K2 IOCG-Type Deposit, Great Bear Magmatic Zone, NWT, with the Carmax Cu-Mo porphyry Deposit, BC'. Unpublished Master's Thesis, Brandon University, Brandon, MB, Canada, 2019.